

## REVIEW ARTICLE OPEN



# Recent research progress on the passivation and selective oxidation for the 3d-transition-metal and refractory multi-principal element alloys

Zening Wang<sup>1</sup>, Yu Yan<sup>1</sup> , Yuan Wu<sup>2</sup> , Yi Zhang<sup>1</sup>, Xinpeng Zhao<sup>1</sup>, Yanjing Su<sup>1</sup> and Lijie Qiao<sup>1</sup>

The wide range of alloy composition controllability for multi-principal element alloys (MPEAs) may provide a great opportunity for discovering special forms of surface oxides to improve the corrosion and oxidation resistance in extreme environments. Changing the type and content of promoting passivation elements would not only change the microstructure of the alloy but also significantly affect the composition and structure of the surface passive film, resulting in a strong impact on the corrosion and oxidation resistance of the alloy. This article reviews recent research on the effects of alloying elements on the passivation properties, the contribution of each alloying element, and the synergistic effect between the elements on the passivation mechanisms and electrochemical dissolution characteristics of surface passive films that form on some MPEAs. In addition, the composition and structural characteristics of surface oxides relevant to the selective oxidation of elements are elaborated upon. Finally, several open questions and recommendations for research directions regarding the passivation and selective oxidation of MPEAs were provided to guide future exploration.

*npj Materials Degradation* (2023)7:86; <https://doi.org/10.1038/s41529-023-00410-0>

## INTRODUCTION

Multi-principal element alloys (MPEAs) have attracted the interest of materials scientists and engineers, who have aimed to investigate their mechanical properties, as well as wear, corrosion, and oxidation resistance. The high number of principal elements in MPEAs will increase the degree of freedom in the alloy composition, especially when non-equiatomic multi-principal elements are considered. Corrosion resistance is a performance index that must be met in the design and development of MPEAs as structural materials. Currently, research on the corrosion behavior of MPEAs has mainly focused on alloy systems composed of transition metal elements. The development of corrosion-resistant MPEAs has mainly considered the alloy composition design, manufacturing method, microstructure, corrosion mechanism, and surface passive film<sup>1–5</sup>. Most studies have focused on the effect of adding alloying elements, such as Cu, Al, Mn, Mo, Ti, Nb, V, and Si, on the corrosion resistance and corrosion mechanisms of CoCrFeNi-based MPEAs<sup>6</sup>. The addition of these alloying elements was found to affect the microstructure and phase structure evolution, thus affecting the corrosion performance of the MPEAs<sup>7–10</sup>. Based on previous research on the corrosion behavior of MPEAs, the addition of alloying elements Cr<sup>11–13</sup>, Mo<sup>8,14</sup>, Co<sup>15,16</sup>, Ni<sup>17,18</sup>, Ti<sup>19,20</sup>, and Nb<sup>21,22</sup> was found to be generally beneficial, as long as no second phase formed, and they were usually present in the passive film. However, the addition of Cu<sup>10,23,24</sup>, Al<sup>25–28</sup>, and Mn<sup>7,29,30</sup> was found to be oftentimes detrimental to corrosion resistance, which was mainly due to the phase transition that produced chemical and structural heterogeneity. The chemical composition of a bulk alloy will determine the composition of the passive film that forms on the alloy surface, especially the enrichment of beneficial elements in the film, thus influencing the initiation process of local corrosion behavior. The oxides that form

on the surfaces of heterogeneities such as the phases of barren Cr element will be less protective and will break down or will undergo preferential dissolution at these regions. Thus, MPEAs with a single-phase structure and uniform distribution of alloying elements will be expected, contributing to enhancing the composition uniformity and structural stability of the passive films<sup>31–33</sup>. MPEAs with refractory elements, such as Ti, Zr, Nb, Ta, Mo, V, W, and Hf, namely refractory multi-principal element alloys (RMPEAs), have mostly simple BCC crystal structures and may also contain some intermetallic phases, mainly B2 and/or Laves<sup>34–39</sup>. Some RMPEAs can maintain stability in the phase structure with increasing alloying elements and heat treatment temperature<sup>40–43</sup>, which will be conducive to maintaining high corrosion resistance. More importantly, these refractory elements will all easily form protective oxides that are thermodynamically stable across a broad range of potential and pH values<sup>44</sup>. Therefore, the characteristics of the passive film that govern the corrosion behavior of the MPEAs include the composition and structure uniformity, compactness, and electronic properties.

MPEAs may form passive films with superior protective properties against corrosion depending on either the presence of large amounts of passivating elements or the formation of specific oxides based on the unusual synergistic effects of alloying elements<sup>45,46</sup>. The high-entropy effect of MPEAs will contribute to achieving a single-phase solid solution, even with the addition of complex elements at a high concentration, which will decrease the occurrence of elemental segregation and favor the formation of a uniform surface passive film. The change in corrosion resistance and the corrosion mechanism of MPEAs can be extensively explored by adjusting the composition and content of alloying elements over a wide range. Passivity models constructed by single functional elements have been developed

<sup>1</sup>Beijing Advanced Innovation Center for Materials Genome Engineering, Corrosion and Protection Center, Key Laboratory for Environmental Fracture (MOE), Institute of Advanced Materials and Technology, University of Science and Technology Beijing, 100083 Beijing, China. <sup>2</sup>State Key Laboratory for Advanced Metals and Materials, University of Science and Technology Beijing, 100083 Beijing, China. ✉email: yanyu@ustb.edu.cn

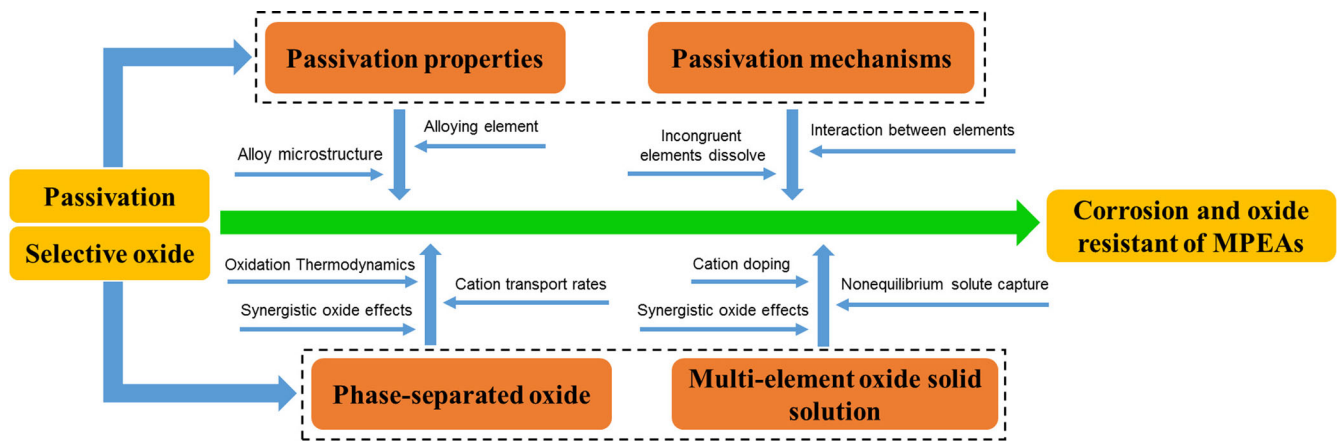


**Fig. 1** The contributions of some research aspects in passivation and selective oxidation to the corrosion and oxide resistance of MPEAs.

for pure metals and conventional single-principal element alloys (SPEAs) but may not be directly available for MPEAs<sup>47</sup>. Beneficial combinations of alloying elements or vacancies may be envisioned to produce synergistic corrosion benefits such as charge distribution<sup>48,49</sup>, passivity promotion and dissolution blocking<sup>50</sup>, the vacancy-mediated diffusion model<sup>51</sup>, and the point-defect model<sup>52,53</sup>. The chemical potential and activity of each alloying element may differ in an MPEA substrate, affecting the passivation and dissolution characteristics of the surface oxides. Thus, determining the contribution of each alloying element to the passivation and dissolution characteristics of MPEAs is essential for understanding the synergistic effect of the alloying elements and the corrosion resistance mechanism of MPEAs<sup>54–56</sup>.

The composition and structure of the surface oxide are also key factors that affect the corrosion resistance of the oxide film, and the presence of multi-elements at high concentrations may affect the formation of surface oxide structures in many ways. The Gibbs free energy of oxide formation of the elements and the transport rate of cations will determine the spatial distribution of elemental fractions in the bulk oxide film<sup>57</sup>. Uneven oxide films with multi-layer structures have been commonly reported in MPEAs composed of transition metal elements, such as NiCr<sub>20</sub>Mo<sub>10</sub><sup>58</sup>, FeCr<sub>15</sub>Ni<sub>15</sub><sup>59</sup>, CrMnFeCoNi<sup>60–62</sup>, CrFeCoNiMo<sup>63</sup>, Ni<sub>38</sub>Fe<sub>20</sub>Cr<sub>22</sub>Mn<sub>10</sub>Co<sub>10</sub><sup>64,65</sup>, and Ni<sub>38</sub>Cr<sub>21</sub>Fe<sub>20</sub>Ru<sub>13</sub>Mo<sub>6</sub>W<sub>2</sub><sup>66</sup> alloys after exposure to air or a solution environment, which was attributed to the selective oxidation behavior of each component at the metal/oxide interface. Selective oxidation can also lead to the enrichment or depletion of some beneficial elements in the oxide film, relative to their concentration in the alloy matrix. In addition to the formation of layered oxide film structures, complicated altered layers will likely exist underneath the oxide film, including modified alloy layers<sup>60,61</sup> with void formation by both vacancy injection and Kirkendall voiding<sup>67</sup>. From the study of pure metals and conventional SPEAs, the surface oxide will generally form the most thermodynamically stable stoichiometric oxide form, based on the phase equilibrium expectations. In the case of MPEAs, superior corrosion or oxidation resistance can also be brought about by the formation of unexpected compositionally complex oxides<sup>68</sup>. More recent work utilizing three-dimensional atom-probe tomography (3D-APT) and transmission electron microscopy (TEM) has confirmed the non-stoichiometric ratios for any alloying elements and oxygen, suggesting that a metastable oxide formed on the MPEAs. The oxides could contain a dominant passivator affected by the other elements, with multiple oxide phases, and the formation of complex multi-cation oxides, which may result in the solid solution forming a highly protective oxide instead of phase-separated stoichiometric oxides. The formation of these multiple oxides was attributed to the occurrence of nonequilibrium solution capture at the interface between the metal and oxides during the growth of the oxide film<sup>69</sup>.

At present, research on the passivation and selective oxidation of MPEAs is in the preliminary exploration stage. Figure 1 illustrates the contributions of some research aspects in passivation and selective oxidation to the corrosion and oxide resistance of MPEAs. However, the role of each element in the formation and growth of a complex oxide, as well as the electrochemical dissolution characteristics, the relative mobility, and reactivity of cations in the oxide film, has remained elusive. Based on recent investigations, this article reviews passivation and selective oxidation and reveals the corrosion resistance of MPEAs associated with their passive film characteristics. The main contents include three aspects: (1) the effect of alloying elements on passivation properties, (2) the contribution of the alloying elements to the passivation mechanisms and electrochemical dissolution characteristics of MPEAs, (3) the composition and structural characteristics of surface oxides due to selective oxidation.

## EFFECT OF ALLOYING ELEMENTS ON PASSIVATION PROPERTIES

The changes in types and contents of alloying elements not only affect the microstructure of MPEAs but also significantly affect the composition and microstructure of the surface passive film, thereby influencing its passivation properties. Based on a thorough assessment of literature reports, the effect of alloying elements on the passivation properties was obtained for some MPEAs, as displayed in Table 1. The role of each alloying element in the stability of passive films on some MPEAs was elaborated as follows.

### Chromium

Cr remains one of the most important alloying elements for improving the corrosion resistance of alloys. Because its passivating character is well-known for conventional SPEAs, it is reasonable to hypothesize that a similar effect could also be produced for MPEAs. A critical concentration of Cr is considered the key to enhancing the corrosion resistance of the alloy. It has been suggested that more than 12–13 at.% of Cr content in Fe–Cr binary alloys will be needed to achieve to complete primary passivation<sup>70,71</sup>. Cr can easily form Cr<sub>2</sub>O<sub>3</sub> due to the lowest free energy of formation, with the content, stability, and distribution in the passive film remarkably influencing corrosion resistance in binary alloys as well as MPEAs<sup>72</sup>.

Shang et al.<sup>73</sup> investigated the passivation properties of equal-atomic NiCo, NiCoCr, NiCoFe and NiCoCrFe alloys in NaCl and HCl solutions. When the Cr element was added to the alloys, the passive region in the polarization curves was considerably

**Table 1.** A summary of alloying elements's effect on the passivation properties of some MPEAs.

Element	Alloy	Solution	Passivation property	The role in passivation	Ref
Cr	NiCo/NiCoFe/NiCoCr/ NiCoFeCr	0.1 M NaCl and 0.1 M HCl	NiCoCr > NiCoFeCr > NiCoCr > NiCoFeCr	Cr can inhibit the dissolution of passive film for NiCoCr and NiCoCrFe alloys.	73
	FeCoNiCr <sub>x</sub> (x = 0, 0.5, 1.0)	0.5 M H <sub>2</sub> SO <sub>4</sub> and 0.6 M NaCl	FeCoNiCr <sub>0.5</sub> > FeCoNi > FeCoNiCr	The excess addition of the Cr element leads to localized corrosion in FeCoNiCr alloy due to the segregation of the Cr element in the interdentrites.	11
	Ni <sub>38</sub> Fe <sub>20</sub> Cr <sub>x</sub> Mn <sub>21-0.5x</sub> Co <sub>21-0.5x</sub> (x = 6, 10, 14, and 22)	0.6 M NaCl	The pitting resistance increases with increasing Cr content.	The alloy with only 6 at.% Cr can still exhibit self-passivation at the open-circuit potential.	12
	Al <sub>0.3</sub> Cr <sub>x</sub> FeCoNi (x = 0–2.0)	0.6 M NaCl	No pitting occurred for the Al <sub>0.3</sub> Cr <sub>x</sub> FeCoNi (x = 1.5–2.0) alloys under the anodic polarization up to 2.0 V <sub>5CE</sub> .	Cr addition results in the increase of the Cr concentration in both the FCC and BCC/B2 phases, leading to the homogeneous passive film enriched in Cr <sub>2</sub> O <sub>3</sub> .	74
Mo	Ultra-fine and coarse-grained CoCrFeMnNi	0.6 M NaCl	Grain refinement leads to reduced pitting resistance.	An inhomogeneous Cr element distribution enhances diffusion of point defects through the passive film that formed in the Cr-depleted regions due to grain refinement.	75
	Ni <sub>78</sub> Cr <sub>22</sub> and Ni <sub>68</sub> Cr <sub>22</sub> Mo <sub>10</sub>	2.0 M H <sub>2</sub> SO <sub>4</sub>	Ni <sub>68</sub> Cr <sub>22</sub> Mo <sub>10</sub> > Ni <sub>78</sub> Cr <sub>22</sub>	Mo enhances the oxidation of Cr to Cr <sub>2</sub> O <sub>3</sub> over Cr(OH) <sub>3</sub>	84
	FeCoCrNiMo <sub>x</sub> (x = 0, 0.1, 0.3, and 0.6)	0.26 M and 1.0 M NaCl	Mo addition enhances the pitting resistance of FeCoCrNi yet preferential localized corrosion occurs in the Mo <sub>0.3</sub> and Mo <sub>0.6</sub> alloys.	1) Mo addition enhances the Cr <sub>2</sub> O <sub>3</sub> /Cr(OH) <sub>3</sub> ratio and Mo oxides in the passive film. 2) The regions depleted in Cr and Mo appeared due to excessive addition in Mo, which results in the inhomogeneous passive film.	8
Mn	(CoCrFeNi) <sub>100-x</sub> Mo <sub>x</sub> (x = 1, 2, 3)	0.6 M NaCl	The pitting resistance increases with the increase of Mo content.	Mo addition increases the MoO <sub>3</sub> in the passive film and improves the stability of the passive film.	14
	Non-equiatomeric AlMnMo	0.6 M NaCl	Mo addition improves the pitting resistance of AlMnMo alloy.	Mo addition reduces the defect density in the passive film.	85
	Non-equiatomeric CrFeCoNiMo	0.05 M H <sub>2</sub> SO <sub>4</sub> + NaCl	Adding Mo up to 10 at.% can significantly improve the pitting resistance.	Cr mainly contributes to the formation of passive film and protection against dissolution, while Mo has a beneficial effect on the passive film resistant to local breakdown.	86
Mn	FeCrNiCoMn <sub>x</sub> (x = 0, 0.3, 0.6, and 1.0)	0.5 M H <sub>2</sub> SO <sub>4</sub>	The corrosion resistance of passive film is improved with the decrease in Mn content.	Mn addition can reduce Cr <sub>2</sub> O <sub>3</sub> in the passive film due to the competitive oxidation of Mn with Cr.	30
	Non-equiatomeric CoFeNiMnCr	0.1 M H <sub>2</sub> SO <sub>4</sub>	Mn addition deteriorates the corrosion resistance.	Mn can increase the chemical dissolution rate of passive films.	7
Co	Al <sub>2</sub> CrFeCo <sub>x</sub> CuNiTi (x = 0, 0.5, 1.0, 1.5, 2.0)	0.5 M HCl	Increasing Co content leads to an enhancement of the corrosion resistance.	Co is conducive to forming Co(OH) <sub>2</sub> that is attached to the surface to prevent the erosion of O <sup>2-</sup> and Cl <sup>-</sup> .	92
	Co <sub>x</sub> CrCuFeMnNi (x = 0.5, 1.0, 1.5, 2.0)	0.6 M NaCl	The alloy with high Co content has improved corrosion resistance.	Co can enhance the stability of Cr <sub>2</sub> O <sub>3</sub> and Ni(OH) <sub>2</sub> in the passive film through the formation of the Co(OH) <sub>2</sub> adsorption layer.	16
	Fe <sub>50</sub> Mn <sub>25</sub> Cr <sub>15</sub> Ni <sub>10-x</sub> Co <sub>x</sub> (x = 0, 5, and 10)	0.6 M NaCl	The corrosion resistance of the alloys decreases with the increase in Co content.	—	94
Co	Ni <sub>52</sub> Ti <sub>48-x</sub> Co <sub>x</sub> (x = 0, 1.5, and 4.0)	0.15 M NaCl	Co-addition increases the corrosion resistance of the alloys.	Co does not affect the composition of the passive film primarily composed of titanium oxide TiO <sub>2</sub>	95
	Fe <sub>40</sub> Ni <sub>20</sub> Co <sub>20</sub> Cr <sub>20</sub>	0.1 M H <sub>2</sub> SO <sub>4</sub>	Non-equiatomeric Fe <sub>40</sub> Ni <sub>20</sub> Co <sub>20</sub> Cr <sub>20</sub> exhibits significantly higher corrosion resistance than the equiatomeric FeMnNiCoCr.	The interaction between Co and other elements can facilitate the formation of Co(Fe,Cr) <sub>2</sub> O <sub>4</sub> oxides with more chemical stability	96

Table 1 continued

Element	Alloy	Solution	Passivation property	The role in passivation	Ref
Al	$Al_x(\text{CoCrFeNi})_{100-x}$ ( $x = 4.5-40$ )	0.6 M NaCl	The corrosion resistance decreases with the increase in Al content.	The increase of the Al content produces more Al oxides/hydroxides and less Cr oxides/hydroxides, thus weakening the compactness of the passive film.	97
	CoCrFeNi/CoCrFeNiAl	0.6 M NaCl	CoCrFeNi > CoCrFeNiAl	Al addition yields the formation of a more defective passive film enriched in $Al_2O_3$ and $Al(OH)_3$	98
	$Al_x\text{CrFeMoV}$ ( $x = 0, 0.2, 0.6, 1$ )	0.6 M NaCl	Al addition reduces the current density in the passive region and does not have an adverse effect on the pitting resistance.	Al addition does not induce the appearance of Al-rich phases, thus leading to the homogeneous passive film	99
Ti	CoNiVAl <sub>x</sub> ( $x = 0, 0.1, 0.2, \text{ and } 0.3$ )	0.6 M NaCl	The corrosion resistance increases with the increase of Al content	Al addition leads to the increase in the atomic ratio of Al/V and $O^{2-}/OH^-$ , thus enhancing the content of metallic oxide in the passive film.	100
	FeCoCrNiAl <sub>x</sub> ( $x = 0.1, 0.3$ )	0.5 M $H_2SO_4$ , 0.5 M HCl	Increasing Al content improves the corrosion resistance in $H_2SO_4$ , while it has a negative effect on the corrosion resistance in HCl.	Increasing Al enhances the oxides/hydroxides ratios of Cr, Fe, and Al, which provides a more compact passive film in $H_2SO_4$ , while $Cl^-$ ions are inclined to combine with the Al-containing metastable ion complexes in HCl.	101
	AlCrFeCoNi/ AlCrFeCoNiTi0.5 FeCoNiCuTi <sub>x</sub> ( $x = 0, 0.2, \text{ and } 0.4$ )	0.6 M NaCl HCl (pH = 3) 0.6 M NaCl	Ti addition significantly improves the pitting resistance. Ti addition enhances the corrosion resistance	Ti addition raises the microstructural heterogeneity and passivation capability. Ti addition promotes the formation of single-phase structures and increases the charge transfer resistance of passive film.	102 105
Nb	CoCrFeNiTi <sub>x</sub> ( $x = 0.1, 0.3, 0.5, \text{ or } 0.7$ )	0.6 M NaCl	As the Ti content increases, the corrosion resistance is improved.	Ti addition provides high energy barriers at the $Cr_2O_3/TiO_2$ interfaces, thus improving the stability of the passive film.	106
	$Ni_{1.5}\text{CrCoFe}_{0.5}\text{Mo}_{0.1}\text{Nb}_x$ ( $x = 0.55, 0.68, \text{ and } 0.8$ )	0.6 M NaCl	The stability of passive film is improved with the increased content of Nb addition.	The improvement in passivation performance is mainly attributed to the reduced point-defect density due to Nb addition.	107
	TiHfZrNb <sub>x</sub> ( $x = 0.2, 0.3, \text{ and } 0.4$ ) $Ti_{30-x}V\text{CrNb}_x$ ( $x = 0, 5, 10, 15, \text{ and } 20$ ) The CoCrFeNiW <sub>x</sub> ( $x = 0.2, 0.5$ )	Hanks' solution 0.6 M NaCl Seawater	As the Nb content increases, the corrosion resistance is continuously enhanced. W addition improves the pitting resistance and passivation properties.	Nb can improve the microstructural homogeneity that ensures a low dissolution rate and a greater resistance of passive film.	108 109
W	$W_x\text{FeCoNiCrMn}$ ( $x = 0, 0.2, 0.4, 0.6, 0.8 \text{ and } 1.0$ )	0.6 M NaCl	The corrosion properties first increase and then decrease with the increase in the W contents.	A small amount of W addition can maintain the continuity of passive film, while excessive W addition produces cohesionless phases that disrupt the continuity of the passive film.	110
	CoCrFeNiZr <sub>x</sub> ( $x = 0, 0.25, 0.5, \text{ and } 1$ )	0.6 M NaCl	The stability of passive film decreases with the increase of Zr content.	1) The thickness of the passive film decreases with the Zr content. 2) Zr-rich phase more easily loses electrons and dissolves during the corrosion.	111
Zr	AlCoCrFeNiZr <sub>x</sub> ( $x = 0, 0.1, 0.2, 0.3, \text{ and } 0.5$ )	0.5 M $H_2SO_4$	The corrosion properties first increase and then decrease with the increase in the Zr contents.	Excessive addition of Zr results in a poor Cr phase, which reduces the continuity of the passivation film and leads to galvanic corrosion.	113

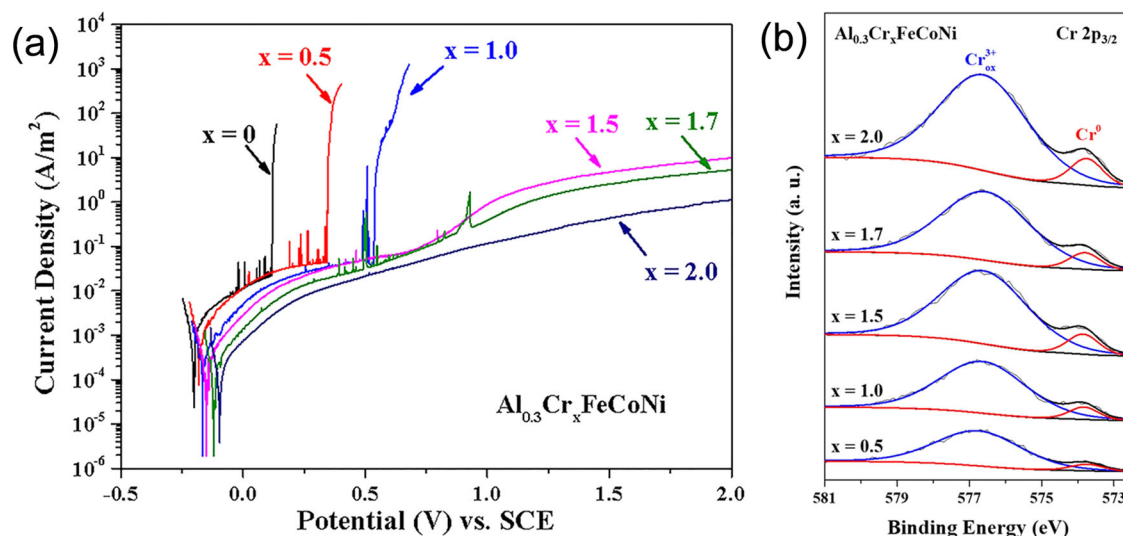


**Fig. 2** The analysis of pitting resistance and chemical composition of passive film on  $\text{Al}_{0.3}\text{Cr}_x\text{FeCoNi}$  ( $x = 0\text{--}2.0$ ) MPEAs. **a** Potentiodynamic polarization curves of the  $\text{Al}_{0.3}\text{Cr}_x\text{FeCoNi}$  ( $x = 0\text{--}2.0$ ) alloys in the 0.6 M NaCl solution, **b** XPS spectra of Cr  $2p_{3/2}$  in the air-formed surface films for the  $\text{Al}_{0.3}\text{Cr}_x\text{FeCoNi}$  ( $x = 0\text{--}2.0$ ) alloys<sup>74</sup>. (Elsevier Copyright, Original Order Number: 501847115, <https://s100.copyright.com/CustomerAdmin/PLF.jsp?ref=9f52b130-a732-4788-83ec-5fe3ca85d13b>).

extended for NiCoCr and NiCoCrFe alloys in the NaCl solution. However, the passive region was not observed for NiCo and NiCoFe alloys in the HCl solution, indicating that the oxides/hydroxides of Ni, Co, and Fe were unstable and dissolved in the HCl solution. Thus, the introduction of Cr could inhibit the dissolution of the passive film for NiCoCr and NiCoCrFe alloys. Chai et al.<sup>11</sup> found that the corrosion resistance of  $\text{FeCoNiCr}_x$  ( $x = 0, 0.5, 1.0$ ) MPEAs with an FCC structure was dependent on the Cr content in  $\text{H}_2\text{SO}_4$  and NaCl solution. The passive film on an equiatomic FeCoNi alloy was composed of  $\text{Fe}_2\text{O}_3$ , NiO, and CoO, which was less stable than the Cr-rich passive film on the  $\text{FeCoNiCr}_{0.5}$  alloy. A further increase in Cr content would increase the segregation of Cr elements in the interdendrites in the FeCoNiCr alloy, deteriorating the corrosion resistance, as a discontinuous state of the passive film on the alloy surface would result from the inhomogeneous distribution of the Cr element in the matrix. Lu et al.<sup>12</sup> prepared  $\text{Ni}_{38}\text{Fe}_{20}\text{Cr}_x\text{Mn}_{21-0.5x}\text{Co}_{21-0.5x}$  ( $x = 6, 10, 14, \text{ and } 22$ ) MPEAs and investigated the effect of Cr content on the corrosion resistance in NaCl solution. The microstructure maintained single-phase FCC with uniformly distributed compositions after solutionization. The pitting resistance of the passive film increased with increasing Cr content, which was confirmed by the increased passivation domain in the potentiodynamic polarization curves. Notably, the alloy with only 6 at.% Cr could still exhibit self-passivation at the open-circuit potential (OCP), despite the Cr content being below the typical reported thresholds.

Yan et al.<sup>74</sup> found that the microstructure of  $\text{Al}_{0.3}\text{Cr}_x\text{FeCoNi}$  ( $x = 0\text{--}2.0$ ) alloys changed from single-phase FCC to FCC + BCC/B2 structures with increasing Cr content in the alloys. The increased Cr content induced a high concentration of Cr over 30 at.% in both the FCC and BCC/B2 phases, which was much higher than the other constituent elements, and the corrosion resistance increased with increased Cr content in the alloys. As shown in Fig. 2a, the alloys with higher Cr content at  $x = 1.5\text{--}2.0$  exhibited no breakdown potential under anodic polarization up to 2.0  $V_{\text{SCE}}$  in the NaCl solution, which was attributed to the formation of passive films enriched in  $\text{Cr}_2\text{O}_3$ , based on X-ray photoelectron spectroscopy (XPS) analysis (Fig. 2b). Han et al.<sup>75</sup> studied the pitting resistance of passive films on ultra-fine grained (UFG) and coarse-grained (CG) CoCrFeMnNi alloys and found that Cr-depleted regions formed in the UFG alloy, whereas a more

homogeneous chromium element distribution was observed in the CG alloy. The enhanced diffusion of point defects through the passive film that formed in the Cr-depleted regions on the UFG alloy occurred easily, thus weakening the stability of the passive film. Huang et al.<sup>76</sup> showed that the Co element could increase the stability of the passive film by inhibiting the hydrolysis of  $\text{Cr}^{3+}$ , while Ni promoted the hydrolysis of  $\text{Cr}^{3+}$ , weakening the stability of the passive film on CoCrNiAlTi alloy in  $\text{H}_2\text{SO}_4$  solutions.

Thus, the change of microstructure due to the introduction of Cr, the content and distribution uniformity of Cr in the passive film, and the influence of other elements coupled with Cr determined the stability of passive films in MPEAs.

### Molybdenum

The enhanced corrosion resistance of stainless steel due to Mo addition has been extensively investigated. Mo-oxides or Mo-oxyhydroxides can inhibit the formation of active sites on passive films, thus impeding the pitting corrosion process<sup>77,78</sup>. Research has also shown that Mo can promote the formation of  $\text{Cr}_2\text{O}_3$  or the enrichment of Cr content in the passive film because Mo can promote the deprotonation of  $\text{OH}^-$  so as to provide  $\text{O}^{2-}$  to enhance the formation of inner Cr oxides<sup>79–83</sup>. Li et al.<sup>84</sup> confirmed the beneficial effects of Mo on the formation of passive films in  $\text{Ni}_{68}\text{Cr}_{22}\text{Mo}_{10}$  alloy through a comparison with an  $\text{Ni}_{78}\text{Cr}_{22}$  alloy and pure Ni and Mo. Mo could facilitate the active-to-passive transition in the low potential domain by comparing the potentiodynamic polarization curves, which were attributed to the enhanced oxidation of Cr to  $\text{Cr}_2\text{O}_3$  over  $\text{Cr}(\text{OH})_3$ , as promoted by Mo addition. Dai et al.<sup>8</sup> studied the effect of Mo content on the corrosion behavior of  $\text{FeCoCrNiMo}_x$  ( $x = 0, 0.1, 0.3, \text{ and } 0.6$ ) MPEAs and found that the addition of Mo could decrease the point-defect density and enhance the  $\text{Cr}_2\text{O}_3/\text{Cr}(\text{OH})_3$  ratio in the passive film on the  $\text{FeCoCrNiMo}_{0.1}$  alloy, which significantly improved the passivation ability compared to the  $\text{Mo}_0$  alloy. However, precipitates were observed in  $\text{FeCoCrNiMo}_{0.3}$  with an increase in the  $\text{FeCoCrNiMo}_{0.6}$  alloys, which induced preferentially localized corrosion at the regions around the precipitates depleted in Cr and Mo. Wang et al.<sup>14</sup> found that the corrosion resistance of the  $(\text{CoCrFeNi})_{100-x}\text{Mo}_x$  ( $x = 1, 2, 3$ ) alloys gradually increased with increasing Mo content. However, the precipitated phases were observed in the  $\text{Mo}_3$  alloy aged at 900 °C, resulting in decreased corrosion resistance. The passive film of the  $(\text{CoCrFeNi})_{100-x}\text{Mo}_x$

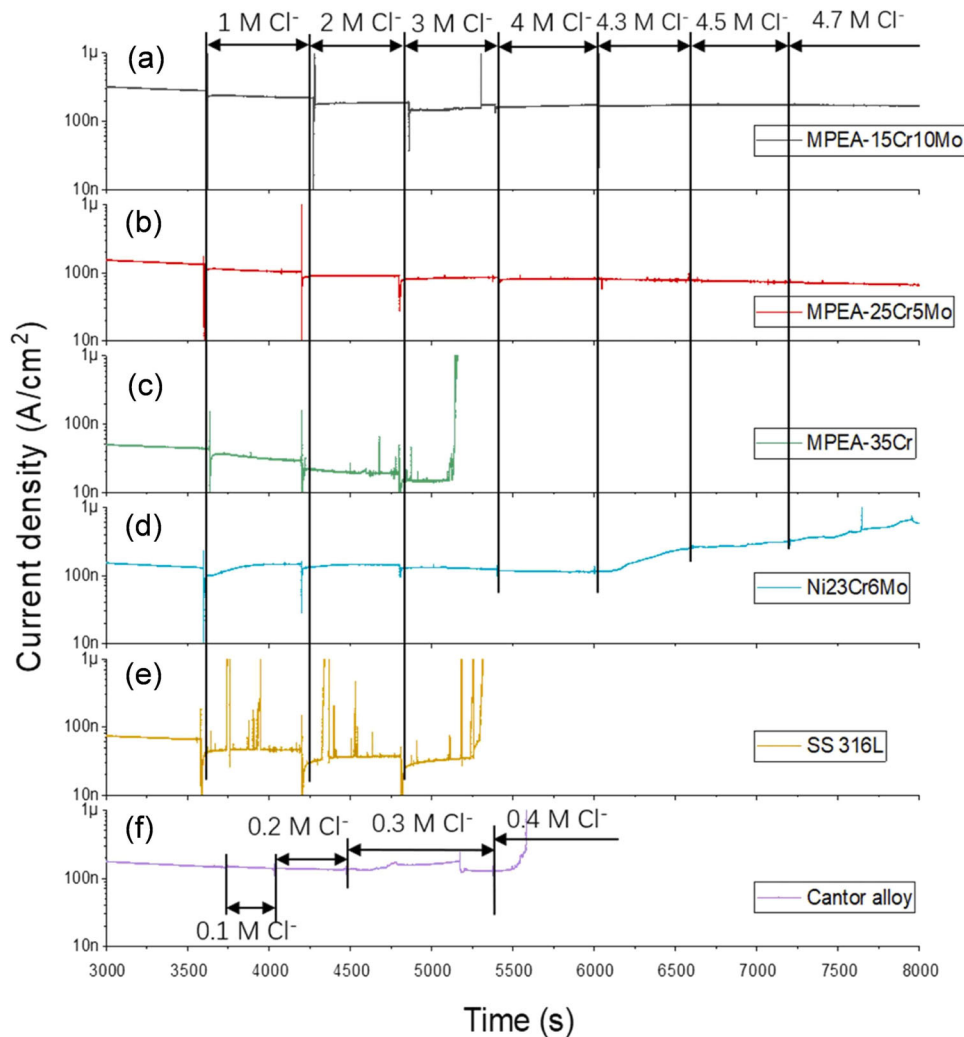


**Fig. 3** Potentiostatic analysis of passivity breakdown and initiation of localized corrosion at  $0 V_{MSE}$  in  $0.05 M H_2SO_4$  with increasing  $Cl^-$  ions concentration for different alloys (chlorides are added after 3600 s of passivation). **a** MPEA- $Cr_{15}Mo_{10}$  ( $Cr_{15}Fe_{10}Co_5Ni_{60}Mo_{10}$ ), **b** MPEA- $Cr_{25}Mo_5$  ( $Cr_{25}Fe_{25}Co_5Ni_{40}Mo_5$ ), **c** MPEA- $Cr_{35}$  ( $Cr_{35}Fe_{20}Co_5Ni_{40}$ ), **d**  $Ni_{71}Cr_{23}Mo_6$  ( $Cr_{35}Fe_{20}Co_5Ni_{40}$ ), **e** 316 L SS, **f** Cantor alloy<sup>86</sup>. (Elsevier Copyright, Original Order Number: 501847644, <https://s100.copyright.com/CustomerAdmin/PLF.jsp?ref=a5f27cf1-813d-4e3a-9705-5bb36c981d95>).

alloys mainly consisted of  $Cr_2O_3$  and  $MoO_3$ , and the interface between  $Cr_2O_3$  and  $MoO_3$  was more susceptible to the cracking of  $Cl^-$  ions. Chen et al.<sup>85</sup> reported that Mo addition significantly improved the pitting resistance of Al-Mn-Mo alloys due to decreased n-type defect density in the passive film. Moreover, molecular dynamics simulations showed that the larger interatomic distance in Al-Mn-Mo compared to Al-Mn led to more Al-O bond formation, resulting in a more compact passive film. Wang et al.<sup>86</sup> investigated the pitting resistance of the passive film on single FCC phase Cr-Fe-Co-Ni-Mo MPEAs with different Mo contents in  $H_2SO_4$  with increasing  $Cl^-$  ion concentration by potentiostatic analysis. As shown in Fig. 3, the alloys without Mo addition, such as  $Cr_{35}Fe_{20}Co_5Ni_{40}$ , 316 L SS, and the Cantor alloy, showed a stable pitting current peak at lower  $Cl^-$  ion concentrations, which was indicative of the initiation of stable pitting once breakdown of the passive film occurred. Notably, no passivity breakdown was observed for the MPEAs containing Mo, even at high  $Cl^-$  ion concentrations, confirming the beneficial effect of the combined alloying of Cr and Mo on the enhanced corrosion resistance of the passive film. Alloying of Cr mainly provided a role in passive film formation and protection against generalized dissolution, as indicated by the negative correlation of the passive current densities with Cr content in these alloys under the

condition of potentiodynamic analysis in pure  $H_2SO_4$  solution. The addition of Mo provided a tremendous beneficial effect on the corrosion properties with the formation of a passive film resistant to local passivity breakdown induced by  $Cl^-$  ion attack.

### Manganese

Manganese is one of the main alloying elements in Co-Cr-Fe-Ni-Mn MPEAs due to its effect on phase stability. Mn has an adverse effect on the corrosion resistance of MPEAs in  $H_2SO_4$  and NaCl solutions. Hsu et al.<sup>30</sup> elucidated the effect of Mn on the passivation behavior of  $FeCrNiCoMn_x$  ( $x = 0, 0.3, 0.6, \text{ and } 1.0$ ) MPEAs in  $0.5 M H_2SO_4$  solution and found that a decrease in Mn addition could provide the improved corrosion resistance of  $FeCrNiCoMn_x$  alloys. Increasing the Mn content will reduce  $Cr_2O_3$  in the passive film due to the competitive oxidation of Mn with Cr, leading to deteriorated corrosion resistance. The effect of Mn on the electrochemical passivation behavior of equiatomic CoFe-NiMnCr,  $(CoFeNi)_{80}Cr_{20}$ ,  $(CoFeNiMn)_{75}Cr_{25}$ , and equiatomic CoFe-NiCr MPEAs in  $0.1 M H_2SO_4$  solution was investigated, which showed that the addition of Mn mainly suppressed the passivation processes and increased the chemical dissolution rate of passive films, as determined by the EIS and potentiodynamic polarization<sup>7</sup>. The detrimental effects of Mn on passive film

stability were caused by the suppression of oxygen or OH<sup>-</sup> adsorption during the passivation process. Mn was found to adsorb oxygen or OH<sup>-</sup> more easily than Cr, forming insoluble compounds<sup>87</sup> or weak and porous oxides<sup>88</sup>, deteriorating the passivity. It has been found that the passive film formed on the equiatomic CrMnFeCoNi alloy was more defective than that formed on the equiatomic CrFeCoNi alloy, which meant that Mn addition facilitated the formation and migration of oxygen vacancies in the passive film<sup>29,89</sup>. However, for other MPEAs, such as Sn<sub>91</sub>Zn<sub>9</sub> alloy, Mn alloying can markedly reduce the donor densities of the passive films and enhance their stability<sup>90</sup>.

### Cobalt

Previous studies have shown that equiatomic CoCr and CoCrMo alloys showed more corrosion resistance than equiatomic NiCr and NiCrMo alloys, respectively, indicating that Co was a strong passivating agent<sup>91</sup>. Qiu et al.<sup>92</sup> found that increasing the Co content resulted in the enhanced corrosion resistance of Al<sub>2</sub>CrFeCo<sub>x</sub>CuNiTi ( $x = 0, 0.5, 1.0, 1.5, 2.0$ ) MPEAs in HCl solution. Zhao et al.<sup>16</sup> showed that the corrosion resistance of the Co<sub>x</sub>CrCuFeMnNi ( $x = 0.5, 1.0, 1.5, 2.0$ ) MPEAs in 0.6 M NaCl solution was enhanced with the increase of Co content, due to the increase in thickness and resistance of the passive films with the increase of Co content. In addition, Co enhanced the stability of Cr<sub>2</sub>O<sub>3</sub> and Ni(OH)<sub>2</sub> in the passive film through the formation of the Co(OH)<sub>2</sub> adsorption layer on the alloy surface<sup>93</sup>. Wei et al.<sup>94</sup> assessed the pitting resistance of Fe<sub>50</sub>Mn<sub>25</sub>Cr<sub>15</sub>Ni<sub>10-x</sub>Co<sub>x</sub> ( $x = 0, 5, \text{ and } 10$ ) MPEAs in NaCl solution. The pitting potential decreased with the increase in Co content, indicating a decrease in pitting resistance due to the increase in grain boundary density in the microstructure. However, the passive film composition was not assessed in detail. Alqarni et al.<sup>95</sup> showed that Co addition enhanced the resistance to uniform and pitting for Ni<sub>52</sub>Ti<sub>48-x</sub>Co<sub>x</sub> ( $x = 0, 1.5, \text{ and } 4.0$ ) MPEAs in NaCl solution. The chemistry of the passive film was not dramatically influenced by Co addition and was primarily composed of TiO<sub>2</sub>. Moreover, the amount of Cl<sup>-</sup> ions that adsorbed on the passive film significantly decreased with Co addition, based on the XPS analysis results. The protective mechanism of the passive film that formed on the non-equiatomic Fe<sub>40</sub>Ni<sub>20</sub>Co<sub>20</sub>Cr<sub>20</sub> MPEAs in 0.1 M H<sub>2</sub>SO<sub>4</sub> was proposed by Wu et al.<sup>96</sup>, based on the XPS results. The study showed that Co cations tended to invade the lattice of (Cr,Fe)<sub>2</sub>O<sub>3</sub> (Fe<sub>2</sub>O<sub>3</sub> or Cr<sub>2</sub>O<sub>3</sub>) and replace trivalent Fe and Cr ions at the octahedral sites, forming some mixed CoCr<sub>2</sub>O<sub>4</sub> and CoFe<sub>2</sub>O<sub>4</sub> oxides with more dense structures and chemical stability, resulting in the formation of a more compact passive film than that formed on the Co-free MPEAs.

### Aluminum

Al is also an element that is prone to forming compact oxide films that decrease the corrosion rate. However, for MPEAs, the introduction of Al can easily cause the formation of multiphase structures and aggravate element segregation in microstructures, thus influencing the stability of passive films<sup>27</sup>. The influence of Al on the microstructure and corrosion resistance of Al<sub>x</sub>(CoCrFeNi)<sub>100-x</sub> ( $x = 4.5-40$ ) thin films was evaluated by Shi et al.<sup>97</sup>. The thin films with a uniform elemental distribution possessed outstanding corrosion resistance, but the resistance decreased with increasing Al content. It was found that increasing the Al content resulted in more Al oxide/hydroxide and less Cr oxide/hydroxide formation, weakening the compactness and protective effect of the passive films. Nascimento et al.<sup>98</sup> compared the pitting resistance of equiatomic CoCrFeNi and CoCrFeNiAl alloys in 0.6 M NaCl solution. The introduction of Al decreased the relative fraction of Cr<sub>2</sub>O<sub>3</sub> and Cr(OH)<sub>3</sub> which are all belong to the p-type semiconducting compounds but enhanced the n-type semiconducting character of the passive film due to the increase in Al oxidized species. Al

addition also yielded the formation of more defective oxides, thus hampering the pitting resistance of surface passive film on the CoCrFeNiAl MPEAs. Raza et al.<sup>99</sup> investigated the pitting resistance of Al<sub>x</sub>CrFeMoV ( $x = 0, 0.2, 0.6, 1$ ) MPEAs and found that the addition of Al did not have an adverse effect on the pitting resistance. This was attributed to the absence of the Cr-depleted and Al-rich BCC phase in the microstructure, favoring the formation of uniform composition distribution in the surface passive film. Recently, the effect of Al addition on the corrosion resistance of CoNiVAl<sub>x</sub> ( $x = 0, 0.1, 0.2, \text{ and } 0.3$ ) MPEAs was investigated<sup>100</sup>, which showed that Al addition decreased the defect density in the passive film, thus improving the corrosion resistance of the CoNiVAl<sub>x</sub> MPEAs. The increase in Al addition also led to the increase of metallic oxide in the film, which was confirmed by the enhanced ratio of Al/V and O<sup>2-</sup>/OH<sup>-</sup>. Fu et al.<sup>101</sup> prepared homogenized FeCoCrNiAl<sub>x</sub> ( $x = 0.1, 0.3$ ) MPEAs with a single-phase structure and uniform element distribution and evaluated their corrosion resistance in HCl and H<sub>2</sub>SO<sub>4</sub> solutions. The increasing Al content enhanced the oxide/hydroxide ratios of Cr, Fe, and Al, which provided a more compact film to resist the dissolution of metal ions in the H<sub>2</sub>SO<sub>4</sub> solution. However, increasing the Al content could enhance the combination of Cl<sup>-</sup> ions with the Al-containing metastable ion complexes, accelerating the dissolution of the MPEAs in the HCl solution.

### Titanium

Wu et al.<sup>102</sup> found that Ti addition raised the microstructural heterogeneity weakening of the local galvanic effect. Moreover, the strong passivation capability of Ti contributed to the formation of a more protective passive film, suppressing the pitting attack on the AlCrFeCoNi MPEAs in NaCl and HCl solutions. The contents of oxidized Cr<sup>3+</sup> and Ti<sup>4+</sup> in the passive film were the main contribution to the improved corrosion resistance of this MPEA system<sup>103</sup>. However, the unoxidized Ti atoms in the passive film were also a considerable factor that was responsible for the improved pitting resistance<sup>104</sup>. Ti addition promoted the formation of single-phase structures for FeCoNiCuTi<sub>x</sub> ( $x = 0, 0.2, \text{ and } 0.4$ ) MPEAs, thus improving the stability of the passive film on the surface<sup>105</sup>. Wang et al.<sup>106</sup> found that Ti addition produced the high energy barriers at the Cr<sub>2</sub>O<sub>3</sub>/TiO<sub>2</sub> oxide interfaces in the passive film, which could increase the energy barriers of adsorption and diffusion for Cl<sup>-</sup> ions.

### Niobium

The effect of Nb addition on the passivation behavior of CoCrNiNb<sub>x</sub> ( $x = 0-0.5$ ) MPEAs in NaCl and HCl solutions were investigated by Wang et al.<sup>21</sup>. The addition of Nb effectively improved the repassivation ability and reduced pitting sensitivity, which was attributed to Nb addition promoting the production of Cr<sub>2</sub>O<sub>3</sub> oxides in the passive film. Moreover, the increase in Nb alloying degree promoted the structural change in the passive film from a single layer to a bi-layer structure with a Cr-enriched outer layer and Nb-enriched inner layer. Wen et al.<sup>107</sup> revealed that the improved passive film stability was mainly attributed to the reduced point-defect density in the passive film of Ni<sub>1.5</sub>CrCoFe<sub>0.5</sub>Mo<sub>0.1</sub>Nb<sub>x</sub> ( $x = 0.55, 0.68, \text{ and } 0.8$ ) MPEAs due to the increased content of Nb addition. Tanji et al.<sup>108</sup> showed that increasing Nb content in the TiHfZrNb<sub>x</sub> ( $x = 0.2, 0.3, \text{ and } 0.4$ ) MPEAs resulted in a greater resistance of the passive film due to decreasing concentration of point defects. Nb had a smaller atomic radius (1.42 Å) than Ti, Hf, and Zr (1.46, 1.57, and 1.60 Å, respectively), which facilitated the mobility and diffusivity of the Nb cations, occupying the formed vacancies, reducing its concentration in the passive film, and maintaining the electrical neutrality of the passive film.

## Tungsten

W addition could also improve the pitting resistance and passivation properties of the  $\text{CoCrFeNiW}_x$  ( $x = 0, 0.2, 0.5$ ) MPEAs in seawater solution<sup>109</sup>. W-added  $\text{W}_x\text{FeCoNiCrMn}$  MPEAs ( $x = 0, 0.2, 0.4, 0.6, 0.8, \text{ and } 1.0$ ) had an improved corrosion resistance referring to the base MPEAs and  $\text{W}_{0.8}$  MPEAs had a best performance. However, for increasing the content of W to 1.0, the cohesionless phases with a large area could not be covered by the passive film, which destroyed the continuity of film and would be as initial sites of pits<sup>110</sup>.

## Zirconium

The opposite effect of Zr addition on the passive film stability of  $\text{CoCrFeNiZr}_x$  ( $x = 0, 0.25, 0.5, \text{ and } 1$ ) MPEAs was verified, which could be related to the content of beneficial oxide in the passive film and the reduced thickness of the passive film, according to XPS analysis<sup>111</sup>. Brito-Garcia et al. found that the pitting resistance of the passive film formed on  $\text{CoCrFeMoNi}$  MPEAs decreased with the addition of Zr due to the increased number of defect points in the passive film<sup>112</sup>. The corrosion properties of the  $\text{AlCoCrFeNiZr}_x$  ( $x = 0, 0.1, 0.2, 0.3, \text{ and } 0.5$ ) MPEAs first increased and then decreased with the increase in the Zr contents in 0.5 M  $\text{H}_2\text{SO}_4$ <sup>113</sup>. A serious galvanic corrosion attack was found for the Al- and Ni-rich, Cr-depleted B2 phases in both the dendrite and interdendrite of the  $\text{Zr}_{0.3}$  alloys.

## PASSIVATION MECHANISMS OF MPEAS

Most studies have mainly focused on the properties and compositions of passive films already formed on the MPEAs, with limited investigations on the formation process of passive films, i.e., the passivation mechanism of MPEAs. The passivity of MPEAs likely consists of a selective oxide process under certain conditions, which is dependent on the specific chemical and electrochemical properties of each alloying element, as well as the interactions with each other<sup>114</sup>. Atomic emission spectroelectrochemistry (AESEC) is an analytical technique that allows for the monitoring of the dissolution of a large number of elements simultaneously and in real-time, during the reaction of MPEAs with an aggressive electrolyte. The fate of each element, whether in metals, oxides, or a solution, during spontaneous dissolution, activation, and passivation could be ascertained by the AESEC technique.

## Ni-Cr-Mo alloys

Lutton et al.<sup>115</sup> studied the kinetics of passivation and dissolution of  $\text{Ni}_{78}\text{Cr}_{22}$  and  $\text{Ni}_{72}\text{Cr}_{22}\text{Mo}_6$  MPEAs in acidic solutions using AESEC coupled with inductively coupled plasma-mass spectrometry (ICP-MS). For the passivation of binary NiCr alloys, initially, significant Ni-rich oxide formation occurred, followed by the continuous build-up of Cr-rich oxides and an increase in preferential Ni dissolution. The dissolutions of Cr and Mo were near their respective limits of detection during passivation, indicating their accumulation of oxides in the passive films of the  $\text{Ni}_{72}\text{Cr}_{22}\text{Mo}_6$  MPEAs. Ni-dissolution was found to almost dominate the dissolution rate of the passive film until the film reached a stable thickness. Henderson et al.<sup>55</sup> found that the spontaneous passivation of non-equiatomic NiCrMo MPEAs was facilitated by the accumulation of mainly Mo-rich as well as Cr-rich oxides after the cathodic activation process in 1 M HCl solution. High Mo content in the alloys was conducive to spontaneous passive film formation, while all elemental dissolution became congruent and the rates increased with time for the alloy with low Mo content, which indicated that an appropriate ratio between the alloyed Cr and Mo must exist to promote the passivation stability. During the subsequent electrochemically assisted passivation processes,

previously accumulated Mo species in the spontaneous passive film were found to be partially removed, while the accumulation of Cr species dominated the film formation process. Li et al.<sup>84</sup> also noticed that the contributions of Cr and Mo changed markedly with the potentials in the active-to-passive transition domain (A1) and the passive domain (A2) during potentiodynamic polarization for the  $\text{Ni}_{68}\text{Cr}_{22}\text{Mo}_{10}$  MPEAs. The Mo(IV) oxides that formed in A1 facilitated the oxidation of Cr to  $\text{Cr}_2\text{O}_3$ , which was possibly considered a step in the nucleation of the passive film, as a high  $\text{Cr}_2\text{O}_3/\text{Cr}(\text{OH})_3$  ratio has been associated with a more protective oxide. Mo was potentially conducive to stabilizing oxygen adsorption, thus rendering the adsorption process more thermodynamically favorable for  $\text{Cr}_2\text{O}_3$  oxide formation<sup>116</sup>. The role of each alloying element during the transpassive dissolution and repassivation process of the non-equiatomic NiCrMo and NiCrMoFe alloys was explored using AESEC in NaCl solution by Henderson et al.<sup>117</sup>. As shown in Fig. 4, Ni was selectively removed from the oxides during transpassive dissolution, while other alloying elements Cr, Mo, and Fe were enriched at least to some extent. Immediately following repassivation, the Mo species that were enriched during transpassive dissolution were released from the surface oxide, while enriched Cr and Fe maintained stability. The researchers also found that the increasing Fe content of the NiCrMoFe alloys could enhance the degree of Mo enrichment and subsequent transpassive dissolution at the surface, which was attributed to the rapid hydrolysis of  $\text{Fe}^{3+}$ , leading to increased local acidification and the promotion of Mo-species deposition.

## Al-Ti-V-Cr alloys

Qiu et al.<sup>52</sup> reported a single-phase Al-Ti-V-Cr MPEA, which exhibited excellent passivity and repassivation behavior in NaCl solution (with  $E_{\text{pit}} > 1.27 V_{\text{SCE}}$ ). The dissolution and repassivation behavior of this MPEA were further investigated in NaCl solution using an AESEC cyclic polarization test by Choudhary et al.<sup>118</sup>. As shown in Fig. 5, Cr, followed by V, underwent preferential dissolution at a higher fraction during anodic polarization, resulting in a surface enriched with Al and Ti just prior to the final breakdown. Subsequently, the dissolution rate of Al increased significantly above  $+1.4 V_{\text{SHE}}$ , leading to a surface that was predominantly enriched with Ti, which in turn could play a major role in repassivation. The dissolution rate of Ti decreased quickly during the reverse potential scan, reaching a negligibly low value and showing rapid repassivation on the alloy surface by the formation of the Ti oxide. This also suggested the highest repassivation ability of Ti among the alloying elements and a greater contribution from Ti in repassivation<sup>119</sup>. XPS analysis also confirmed that the fraction of  $\text{TiO}_2$  in the passive film increased during the transpassive dissolution of V and Cr. The dissolution of  $\text{V}_2\text{O}_3$  and  $\text{Cr}_2\text{O}_3$  would also increase the defect density in the passive film, thus providing an easy path for the oxygen to migrate in, and assist in the growth of stable  $\text{TiO}_2$ . Moreover, the transpassive dissolution reactions of  $\text{V}_2\text{O}_3$  and  $\text{Cr}_2\text{O}_3$  led to the localized acidification of the adjacent electrolyte by releasing the protons, which could also increase the dissolution kinetics of  $\text{Al}_2\text{O}_3$ <sup>120</sup>. Qiu et al.<sup>119</sup> also found that Al dissolution was 1–2 orders of magnitude greater than V, Cr, and Ti for nonequiatomic  $\text{Al}_{1.5}\text{TiVCr}$  MPEAs in NaCl solutions. The dissolution rate of Al was found to decrease with increasing fractions of  $\text{Cr}_2\text{O}_3$ ,  $\text{TiO}_2$ , and  $\text{V}_2\text{O}_3$  oxides in the passive film of AlTiVCr.

## Co-Cr-Fe-Ni-Mn alloys

Luo et al.<sup>121</sup> employed the AESEC approach to investigate the overall dissolution rate of the equiatomic  $\text{CoCrFeMnNi}$  MPEAs in 0.1 M  $\text{H}_2\text{SO}_4$  solution. The researchers found that no obvious selective dissolution of Mn, Co, Ni, and Fe occurred during passivation on the MPEAs, resulting in Cr content in the passive film that was much lower than that in the 304 SS passive film. Han

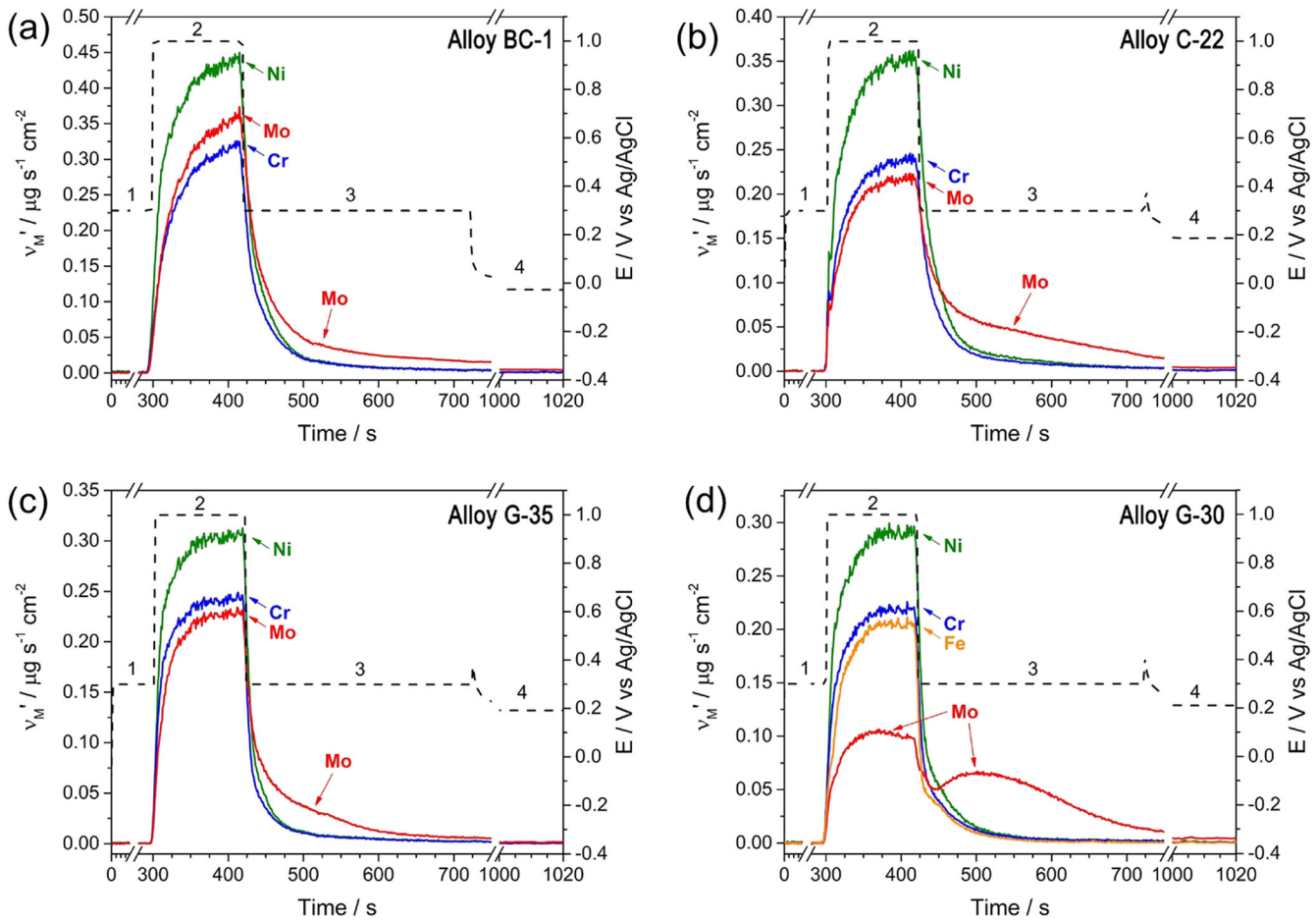


**Fig. 4** Normalized dissolution rates of the non-equiatom NiCrMo and NiCrMoFe MPEAs, during potentiostatic polarization experiments in NaCl solution at 75 °C. **a** BC-1( $\text{Ni}_{63}\text{Cr}_{15}\text{Mo}_{22}$ ), **b** C-22( $\text{Ni}_{65}\text{Cr}_{22}\text{Mo}_{13}$ ), **c** G-35( $\text{Ni}_{58.7}\text{Cr}_{33.2}\text{Mo}_{8.1}$ ), **d** G-30( $\text{Ni}_{49.5}\text{Cr}_{30}\text{Mo}_{5.5}\text{Fe}_{15}$ )<sup>117</sup>. (Elsevier Copyright, Original Order Number: 501847117, <https://s100.copyright.com/CustomerAdmin/PLF.jsp?ref=22d7a21a-03af-4d5c-b550-a89f307b015d>).

et al.<sup>54</sup> focused on non-equiatom Ni<sub>38</sub>Fe<sub>20</sub>Cr<sub>22</sub>Mn<sub>10</sub>Co<sub>10</sub> MPEAs and tracked the fate of each alloying element during linear sweep voltammetry in a slightly acidified chloride solution. Ni was found to dissolve into the solution and only minor or trace amounts of Fe and Co were incorporated into the oxides or hydroxides at low concentrations. Both Cr and Mn enrichment occurred during the active-to-passive transition and the complete passive regions, reflecting that Mn contributed to the surface film. Potentiostatic polarization indicated that Mn dissolved congruently with Cr enrichment at a lower anodic passive potential, whereas significant enrichment of Mn was observed at a higher anodic passive potential. In addition, Cr enrichment occurred in the early stage of passivation, while Mn accumulation was much greater as a function of time compared to Cr<sup>64</sup>. Han et al.<sup>114</sup> also found that the selective dissolution rate of Mn increased with time at an applied potential in the passive potential domain, while the other alloying elements showed typical passivation trends for Ni<sub>38</sub>Fe<sub>20</sub>Cr<sub>22</sub>Mn<sub>10</sub>Co<sub>10</sub> MPEAs in the 2 M H<sub>2</sub>SO<sub>4</sub> solution, showing a less stable and high dissolution rate of the formed Mn-based passive film.

Dworschak et al.<sup>122</sup> studied the electrochemical passivity characteristics of a library of alloys, spanning from equiatom binary alloys up to equiatom NiCoCrFeMn MPEAs using normal pulse voltammetry (NPV) combined with ICP-MS in NaCl solution. As shown in Fig. 6, with higher Ni, the Fe-anodic dissolution peak from equiatom NiCoFeMn MPEAs demonstrated difficulty establishing stable passivity at a high anodic potential, which

showed that the Fe and Ni-induced oxide film was less pronounced, if no Cr was present. Fe showed a low anodic dissolution rate with time and a pronounced cathodic peak profile, indicating that its oxide could be deposited at applied anodic potentials and stripped at negative potentials in equiatom NiCoCrFe MPEAs. No significant Cr anodic dissolution was observed, even if high anodic potential was applied. This slow current evolving profile at higher polarizations from anodic to cathodic transition was indicative of delayed Cr-dissolution after polarization switching, which corresponded to the initiation of cathodic Fe dissolution. This confirmed the synergistic stabilizing effect of Fe and Cr in the passive film, where moderated and delayed Fe dissolution resulted in a gradient of Fe with increased concentration at the oxide/liquid interface and which delayed Cr-dissolution, leading to enriched Cr at the metal/oxide interface. However, anodic dissolutions for Cr and Fe at high applied potentials were more significant for equiatom NiCoCrFeMn MPEAs. Mn addition was found to effectively change the Fe dissolution pattern from cathodic to anodic transition, thus catalyzing the dissolution of the Fe/Cr layer and preventing the formation of stable oxides.

#### COMPOSITION AND STRUCTURES OF SURFACE OXIDE

The inhomogeneous oxide structure in MPEAs, such as lamellar characteristics and embedded oxide structure, have been verified by scanning transmission electron microscopy (STEM), 3D-APT,

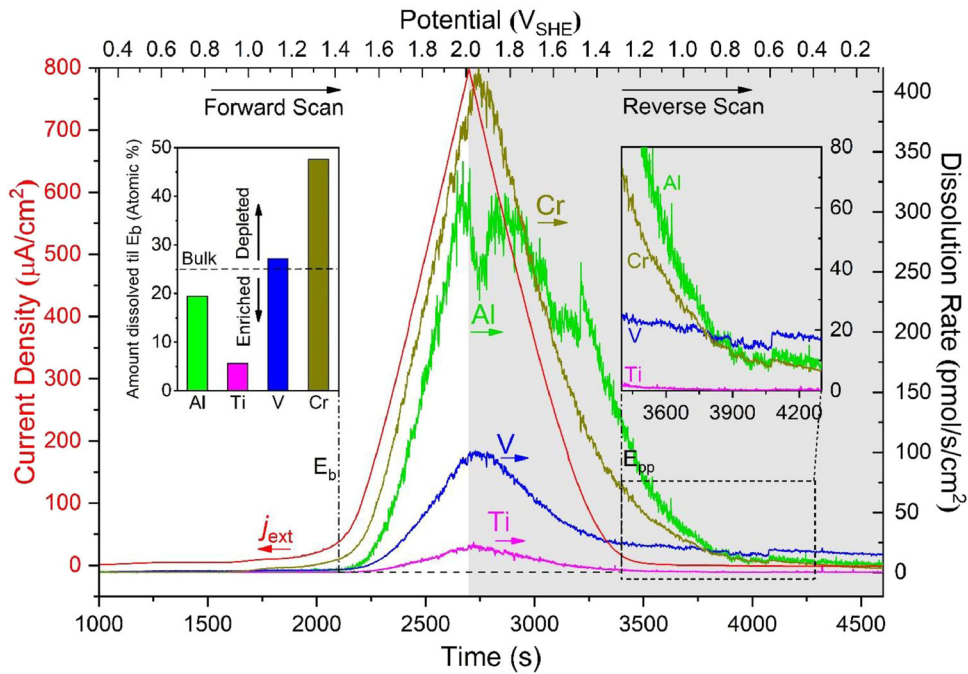


**Fig. 5** AESEC cyclic polarization curve revealing incongruent dissolution behavior of AlTiCr, during forward followed reverse potential scan<sup>118</sup>. (Elsevier Copyright, Original Order Number: 501847120, <https://s100.copyright.com/CustomerAdmin/PLF.jsp?ref=9e393be0-5665-44c3-98fd-dfad797de871>).

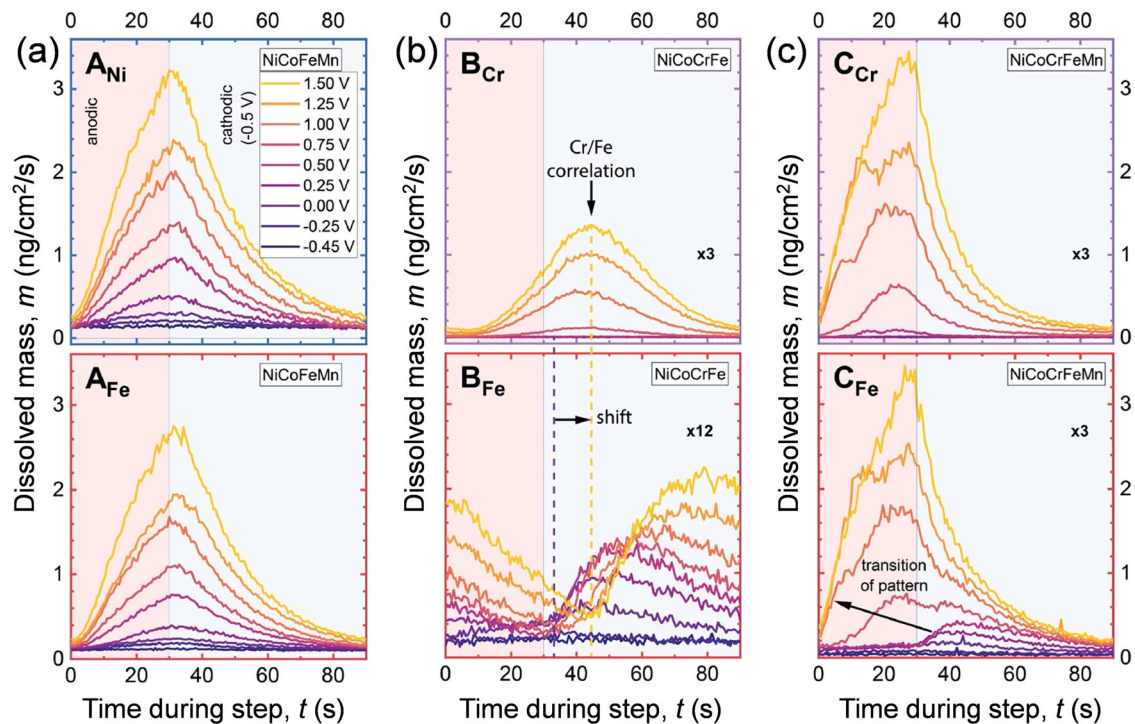


**Fig. 6** Elemental dissolution profiles of Fe (red outline) comparing with Ni (blue outline) and Cr (purple outline) in normal pulse voltammetry sequence. **a** NiCoFeMn, **b** NiCoCrFe, **c** NiCoCrFeMn stacked with selected step potentials. Anodic polarization (red shading) at rising potentials is followed by reconditioning potential at  $-0.5 V_{Ag/AgCl}$  (cathodic polarization)<sup>122</sup>. (Elsevier Copyright, Original Order Number: 501847128, <https://s100.copyright.com/CustomerAdmin/PLF.jsp?ref=c47416c4-5442-4031-b5d6-0d8037fd3f7c>).

and time-of-flight secondary ions mass spectrometry (TOF-SIMS). The occurrence of selective oxidation due to the significant differences in Gibbs free energy of oxide formation of the elements and the transport rate of cations can prompt the uneven

distribution of elements in space, thus resulting in the inhomogeneous oxide structure. In addition, the solid solution of cations in other elemental oxides and cation dopants can lead to the formation of complex multi-element oxides. For the MPEAs, multi-

element oxides containing many elements within one phase instead of phase-separated stoichiometric oxides were confirmed by STEM and 3D-APT. According to the driving force for oxidation of elements in the MPEAs, they are mainly divided into naturally formed oxide, electrochemically grown oxide, and high-temperature formed oxide.

### Native oxide

Recently, Sasidhar et al.<sup>123</sup> performed high-resolution structural and chemical characterization of the native oxide film that formed on a Fe<sub>87</sub>Cr<sub>13</sub> alloy. This steady-state oxide film was enriched with Cr at the oxide/metal interface and depleted in Cr at the oxide/environment interface, which was attributed to the higher mobility of the Fe<sup>3+</sup> cations compared to Cr<sup>3+</sup> cations, leading to a greater extent of Fe<sup>3+</sup> cation diffusion through the Cr-enriched oxides and accumulation at the oxide/environment interface. Zhang et al.<sup>59</sup> observed the growth process of a native oxide film on a ternary FeCr<sub>15</sub>Ni<sub>15</sub> alloy, where the initial oxide consisted of a layer of amorphous Cr-rich oxide. Subsequently, the dominant outward diffusion of Fe yielded a bi-layer structure with an inner Cr-rich layer and an outer Fe-rich layer. The native oxide layer was consistent with the early stages of oxidation of high-temperature oxides in the FeCr<sub>18</sub>Ni<sub>14</sub> alloy<sup>124</sup>. With long-term aging in air, the amorphous oxide first turned to a crystalline NaCl-structured Cr<sub>2</sub>O<sub>3</sub>-FeO mixture, and then, Fe<sup>2+</sup> at the outer layer was oxidized to higher valence Fe<sup>3+</sup>, causing the NaCl structure to partially transform into a spinel structure. Moreover, Cr<sub>2</sub>O<sub>3</sub> further oxidized to the higher valence state of CrO<sub>3</sub>, forming the outermost amorphous oxide layer. Adjacent to the oxide film/matrix interface, a Ni enrichment layer would always exist. Wang et al.<sup>60</sup> investigated the compositions of native oxides and passive films of equiatomic CoCrFeMnNi MPEAs using TOF-SIMS and XPS. A duplex passive film formed on the substrate, where Fe and Co were located preferentially in the outer layer, Mn was in the inner layer, and Cr was distributed in the entire film. A modified alloy layer, enriched in Ni, was observed under the oxide film.

The native oxide films of amorphous Cu<sub>x</sub>Zr<sub>1-x</sub> ( $x = 0.33, 0.5, 0.67,$  and  $0.75$ ) alloys were studied by Xu et al.<sup>125</sup>. A thin ZrO<sub>2</sub> film formed on top of the amorphous alloys due to a higher affinity for oxygen, with a Cu-enriched alloy layer located below and tetragonal ZrO<sub>2</sub> nucleates located between the oxide film and the alloy. For the alloys with dominant Cu content, the Cu atoms with a smaller atomic radius that diffused faster to the surface and reacted with oxygen gradually formed an amorphous Cu<sub>2</sub>O layer on top of the oxide film, with an amorphous ZrO<sub>2</sub> oxide layer below. The researchers further studied the oxidation mechanism of Cu<sub>x</sub>(Zr<sub>0.67</sub>Al<sub>0.33</sub>)<sub>100-x</sub> ( $25 \leq x \leq 50$ ) amorphous alloys at high temperatures<sup>126</sup>. Native surface oxides on Cu<sub>47</sub>Zr<sub>45</sub>Al<sub>8</sub> metallic glassy formed under ambient conditions, which were observed by aberration-corrected STEM<sup>127</sup>, and consisted of dominant Al<sub>2</sub>O<sub>3</sub> and ZrO<sub>2</sub> amorphous oxides with homogeneously embedded crystalline Cu<sub>2</sub>O nanoparticles that formed at the metallic glass/oxide interface and were attributed to the much lower formation Gibbs free energies of Cu<sub>2</sub>O ( $-110 \text{ kJ mol}^{-1}$ ) than that of ZrO<sub>2</sub> ( $-990 \text{ kJ mol}^{-1}$ ) and Al<sub>2</sub>O<sub>3</sub> ( $-1580 \text{ kJ mol}^{-1}$ ). Single-phase amorphous Zr-Al-O films with a fixed stoichiometric composition of (Zr<sub>0.67</sub>Al<sub>0.33</sub>)O<sub>1.83</sub> formed on the top of the alloys with relatively low Cu alloying content. However, for alloys with relatively high Cu content, the relatively strong chemical interactions of Cu with Al reduced their atomic mobilities compared to Zr, leading to immobilized Cu and Al by the nucleation of tiny intermetallic precipitates in the Cu-enriched zone directly behind the oxide growth front. Thus, only Zr was preferentially oxidized to form ZrO<sub>2</sub> at the outer layer. In addition, Mendis et al.<sup>128</sup> studied the oxidation of Ti<sub>100-x</sub>Ta<sub>x</sub> alloys ( $x = 10, 20, 30, 50, 60$  and  $75$ ) alloys and found that the volume fraction of Ta measured in the underlying substrate was consistently higher than its nominal

fraction in the bulk alloy. This suggested that the oxidation of Ta was inhibited due to the preferential oxidation of Ti. As more Ti was depleted due to preferential oxidation, the dealloying layer under the oxide film became Ta-rich, allowing for the formation of Ta-rich oxides<sup>129</sup>. As indicated by the above research, the lamellar characteristics of the oxide film components of the MPEAs were the result of selective oxidation of the constituent elements, which was related to the oxidation Gibbs free energy of the constituent elements, the migration rate of the cations, the interactions between the constituent elements, and the formation of special alloy phases due to the dealloying process.

### Electrochemically grown oxide

Gerard et al.<sup>130</sup> characterized the passive films formed on the non-equiatomic Ni<sub>38</sub>Fe<sub>20</sub>Cr<sub>10</sub>Mn<sub>17</sub>Co<sub>17</sub> MPEA during potentiostatic hold experiments with 3D-APT, as shown in Fig. 7. An obvious enrichment of Cr and Mn was observed in the outer layer, and an accumulation of Fe and Co was observed within the inner oxide. Enrichment of Ni within the altered zone at the metal/oxide interface and altered zone could be found. Kim et al.<sup>131</sup> found that the lower corrosion resistance of austenitic stainless steels (Fe<sub>64</sub>Cr<sub>18</sub>Mn<sub>18</sub>) compared to 304 and 316 stainless steels was due to their instability in the passive film structure. As shown in Fig. 8a, the STEM image and corresponding Energy Dispersive Spectrometer (EDS) maps showed that nanocrystalline MnO oxides were embedded in the passive film subjected to the potentiodynamic polarization test. The High Resolution Transmission Electron Microscope (HRTEM) image of MnO and the corresponding Fast Fourier Transform (FFT) pattern confirmed that the crystal structure of MnO had a hexagonal wurtzite structure (Fig. 8b, c). Cracks or pores were observed in the vicinity of MnO, which potentially deteriorated the passive film stability. While adding Mo and Ni, which could reduce the density of MnO by absorbing oxides, the presence of embedded nanocrystalline oxides possibly facilitated the local short-circuit diffusion of oxygen through the grain boundaries to the base alloy and the outward diffusion of cations, thus potentially influencing elemental redistribution, particularly Mn, as demonstrated in a previous study for Cantor alloys<sup>57</sup>. Zhang et al.<sup>132</sup> showed that some nanocrystalline oxides were embedded in the amorphous passive film that formed on FeCr<sub>15</sub>Ni<sub>15</sub> single-crystal alloys in chloride-containing media. The energy barriers for Cl<sup>-</sup> ion diffusion from one oxygen vacancy to its neighboring one were the lowest at the interfacial region than in the interior of the amorphous or nanocrystalline oxides.

Rost et al.<sup>133</sup> confirmed the formation of single-phase structure oxides when five equiatomic binary oxides were mixed, such as MgO, CoO, NiO, CuO, and ZnO. Moreover, all cation distributions were proven to be random and homogeneous (Fig. 9), which showed that many elements could be substituted on a single sublattice and that a host structure could be retained even when adding elements that formed different crystal structures<sup>134,135</sup>. Yu et al.<sup>69</sup> studied the oxide compositions and structures that formed on Ni<sub>72</sub>Cr<sub>22</sub>Mo<sub>6</sub> MPEAs during both high-temperature oxidation and aqueous corrosion. The researchers verified the presence of rock salt (Cr<sub>1-x</sub>Ni<sub>x</sub>O<sub>1.5-x/2</sub>) or corundum (Cr<sub>2-x</sub>Ni<sub>x</sub>O<sub>3</sub>) structure oxides close to the alloy/oxide interface, and the chemical composition was far from equilibrium (Fig. 10a). The formation of non-stoichiometric oxides was the result of nonequilibrium solute capture at the moving oxidation fronts, as illustrated in Fig. 10b. The velocity of physical interfacial motion achieved by the cations and vacancies moving into the oxides was significantly larger than the interfacial diffusion coefficient of the cations, resulting in local equilibrium breakdown at the interface and the formation of metastable multi-element oxide solid solutions. The metastable oxide solid solutions were possible across the entire

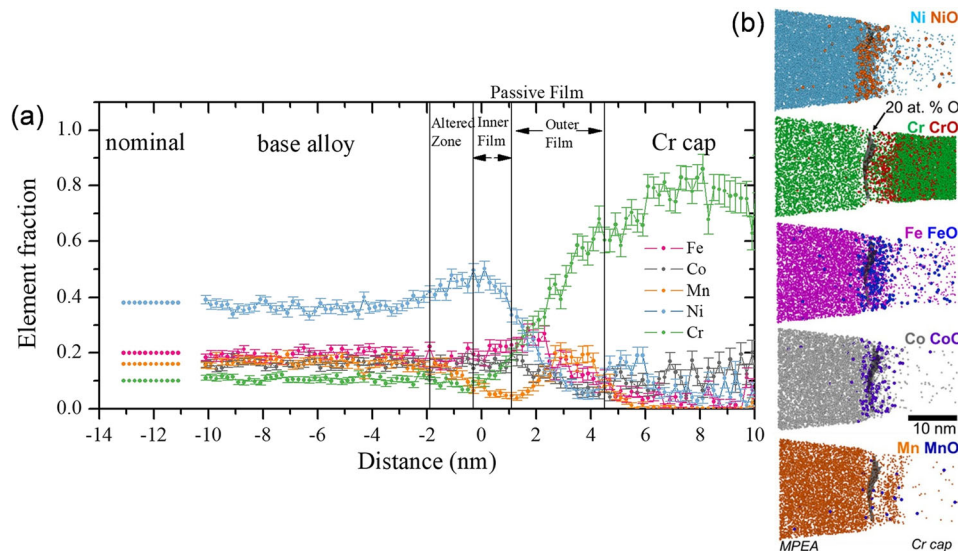


**Fig. 7** 3D-APT element analysis of the electrochemically formed passive film on  $\text{Ni}_{38}\text{Fe}_{20}\text{Cr}_{10}\text{Mn}_{17}\text{Co}_{17}$  MPEA during potentiostatic hold at  $0 \text{ V}_{\text{SCE}}$  for 10 ks in deaerated  $\text{NaCl} + \text{HCl}$  solution. **a** The concentration profile (the standard error  $\sigma$  in the concentration profiles is defined as:  $\sigma = \sqrt{c_i(100 - c_i)/N_T}$ , where  $c_i$  is the local concentration of species  $i$ , and  $N_T$  is the total number of atoms in the concentration measurement), **b** The 3D element distribution maps<sup>130</sup>. (Elsevier Copyright, Original Order Number: 501847135, <https://s100.copyright.com/CustomerAdmin/PLF.jsp?ref=f6716687-7122-49d4-810f-151cbfeb59e9>).

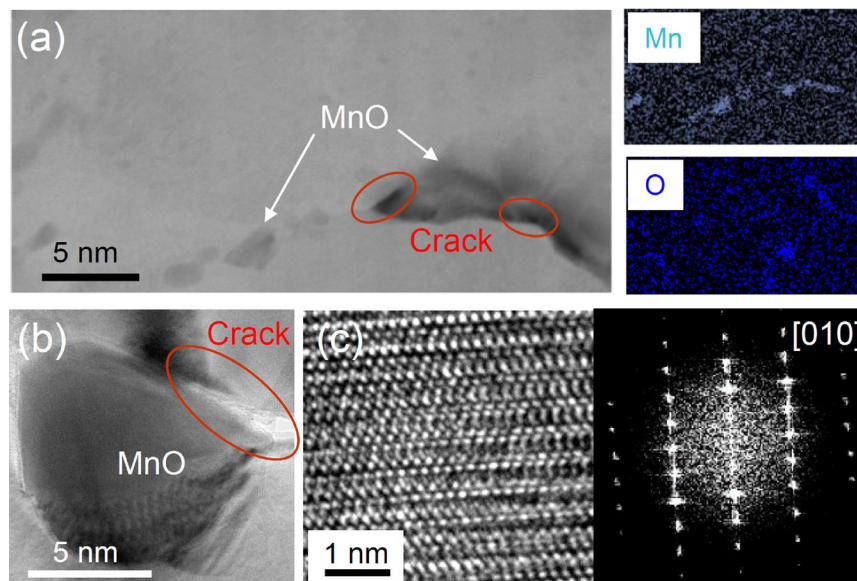


**Fig. 8** TEM characterization of microstructure for the passive film on the austenitic stainless steels ( $\text{Fe}_{64}\text{Cr}_{18}\text{Mn}_{18}$ ). **a** TEM image of the passive film on the  $\text{Fe}_{64}\text{Cr}_{18}\text{Mn}_{18}$  subjected to potentiodynamic polarization test, and corresponding EDS maps of Mn and O, **b** TEM image of MnO, showing crack formation at the interface between the pre-existing MnO and surrounding oxide, **c** HRTEM image of MnO, corresponding FFT pattern and Fourier Transform fringes (bottom) under [010] zone axis, revealing hexagonal wurtzite  $\text{MnO}$ <sup>131</sup>. (Open access article, no permission is required to use this article, <https://s100.copyright.com/AppDispatchServlet?publisherName=ELS&contentID=51359646221003924&orderBeanReset=true>).

compositional range, which was a function of the interfacial velocity.

The potentiostatically formed passive film on the  $\text{Al}_{0.3}\text{Cr}_{0.5}\text{Fe}_2\text{Mn}_{0.25}\text{Mo}_{0.15}\text{Ni}_{1.5}\text{Ti}_{0.3}$  MPEAs were found to be enriched in Ti, Cr, and Al using XPS analysis by Inman et al.<sup>136</sup>, as shown in Supplementary Fig. 1a, b. It was found that the existence of complex Al, Cr, and Ti containing solid solution oxides, such as  $\text{Ti}_2\text{CrO}_5$  and  $\text{TiAl}_2\text{O}_5$  that are suggested to potentially be stable from thermodynamic calculations, as illustrated by the convex-hull diagrams in Supplementary Fig. 1c, d. Quiambao et al.<sup>68</sup> showed that an oxide containing all elements in the bulk  $\text{Ni}_{38}\text{Cr}_{21}\text{Fe}_{20}\text{Ru}_{13}\text{Mo}_6\text{W}_2$  alloy in a

non-equilibrium, non-stoichiometric solid solution formed without distinct phase separation into single-element oxide phases during potentiostatic potential passivation. Meanwhile, the oxide film showed significant enrichment in Cr and Ru, with Mo and W near their bulk composition, and the depletion of Fe and Ni due to selective dissolution at the solution/oxide interface. The enrichment of Cr and Ru in the oxides was due to the significant dissolution of Ni, Fe, Mo, and W at rates approximately proportional to their bulk concentrations.

This meant that the formation process of the multi-element oxide solid solutions on the MPEAs in the aqueous solutions was

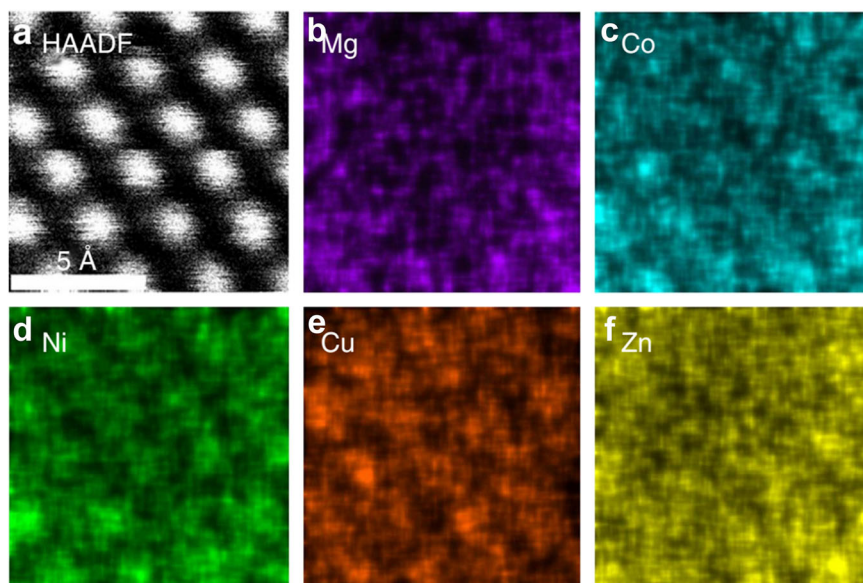


**Fig. 9** STEM-EDS analysis of an oxide system consisting of an equiatomic mixture of MgO, CoO, NiO, CuO, and ZnO. **a** High-angle annular dark field (HAADF) image shows the arrangement of atomic structure for the mixed oxide. The individual EDS maps show uniform spatial distributions for **b** Mg element, **c** Co element, **d** Ni element, **e** Cu element, and **f** Zn element<sup>133</sup>. (Open access article, no permission is required to use this article, <https://s100.copyright.com/AppDispatchServlet?title=Entropy-stabilized%20oxides&author=Christina%20M.%20Rost%20et%20al&contentID=10.1038%2Fncmms9485&copyright=The%20Author%28s%29&publication=2041-1723&publicationDate=2015-09-29&publisherName=SpringerNature&orderBeanReset=true&oa=CC%20BY>).

likely controlled by a combination of thermodynamics and kinetics. According to thermodynamic databases for multicomponent systems based on the methodology known as the CALculation of PHase Diagram (CALPHAD), some of the oxide solid solution phases, i.e., corundum (Fe,Cr)<sub>2</sub>O<sub>3</sub>, spinel (Fe,Ni,Cr,Mn,Co)<sub>3</sub>O<sub>4</sub>, cubic (Co,Fe)<sub>2</sub>O<sub>3</sub>, and (Ni,Mn)<sub>2</sub>(Ni,Mn,O)<sub>3</sub> phases, that formed on Ni<sub>38</sub>Fe<sub>20</sub>Cr<sub>22</sub>Mn<sub>10</sub>Co<sub>10</sub> were found to be thermodynamically stable for the low Gibbs energy of formation of the compounds over large portions of the E-pH diagram, as shown in Supplementary Fig. 2<sup>44</sup>. The enrichment or depletion of select elements was dependent on the details of the various rate-determining processes, such as selective oxidation at the metal/oxide interface, preferential dissolution of the cations and redeposition rate combined with the oxygen and oxyhydrogen ions at the solution/oxide interface, and the differential ionic transport rates across the oxides. Gerard et al.<sup>64</sup> found that much greater enrichment of Cr in the oxide occurred to a greater extent in the Ni<sub>38</sub>Fe<sub>20</sub>Cr<sub>22</sub>Mn<sub>10</sub>Co<sub>10</sub> alloy than in the Ni<sub>76</sub>Cr<sub>24</sub> binary alloy, for which selective dissolution did not fully explain the observed Cr enrichment. The unusual combination of multiple vacancy sources came from the different rates of vacancy-mediated transport as a result of the dissolution of multiple elements, and the differences in the interfacial or surface reaction rates may have enhanced the transport of Cr to the metal/oxide interface, which could have contributed to the observed Cr enrichment.

### High-temperature formed oxide

The oxide films formed at high temperatures have semiconductor characteristics similar to that of the electrochemically grown oxide films<sup>137</sup>. The semiconductor properties of oxide films are determined by their composition and structure, which is expected to be crucially important in studying the protective characteristics against corrosion. In addition, the surface oxide formed in the air at high temperatures presents great thickness, which is beneficial for characterizing its microstructure and can help in understanding the transport characteristics of cations and oxygen. Consequently, it is necessary to gain a detailed perception of the structural and compositional information of the oxide films

formed at high temperatures for a comprehensive understanding of the growth mechanisms behind the electrochemically grown oxide films.

The oxide film of the ternary Ni<sub>76</sub>Cr<sub>16</sub>Fe<sub>8</sub> alloy after oxidation at 350 °C consisted of a duplex structure: an inner Cr-rich layer and an outer layer that was rich in Ni and Fe, and the inner layer from pure Cr<sub>2</sub>O<sub>3</sub> toward spinel (NiCr<sub>2</sub>O<sub>4</sub>)<sup>138</sup>. Li et al.<sup>60</sup> analyzed the elements distribution throughout the oxide films on nanocrystalline CrMnFeCoNi thin films exposed to air at 500 °C for 5 min using 3D-APT. Mn and Cr oxides formed on the top of the oxide film, suggesting outward diffusion through the high-density grain boundaries and triple junctions supplying the shortest diffusion path. The resultant high concentration of Fe and Co, as well as reduced Ni content, led to decomposition at the oxide/alloy interface and the formation of the FeCo-rich B2 phase, which potentially accelerated the outward diffusion of Mn and Cr, as shown in Supplementary Fig. 3. From the above research results, it could be seen that the composition and elemental distribution of the oxide film would be affected by the composition ratio, microstructure and oxidation methods of MPEAs.

Yu et al.<sup>67</sup> investigated the early-stage oxidation of an equiatomic CoCrFeNi alloy and found that the formation of multi-element oxide solid solutions was dependent on the competition between thermodynamics and kinetics involving the relative diffusion rate of the cations and oxygen. As shown in Supplementary Fig. 4, the oxide layers consisted of inner corundum and outer spinel structures, which were determined by electron diffractions. The EDS compositional line scan showed that Ni was abundant at the metal/oxide interface, while Cr and Fe were depleted. Cr dominated in the corundum layer, and Fe, Co, and Ni were rich in the spinel phase (Supplementary Fig. 4b). The dominant oxygen transport in the Cr-rich corundum led to inward growth of the corundum phase. The growth of the Fe-rich spinel oxides with Co and Ni dopants was dominated by outward cation diffusion. The diffusion of Fe and Co in the corundum solid solution was significantly faster than that of the host Cr cations, as the Gibbs energy of formation of Cr<sub>2</sub>O<sub>3</sub> was significantly lower than that of Fe<sub>2</sub>O<sub>3</sub> and Co<sub>2</sub>O<sub>3</sub>, meaning higher permeability of Fe and Co in the corundum phase. Yu et al.<sup>139</sup> also found that the

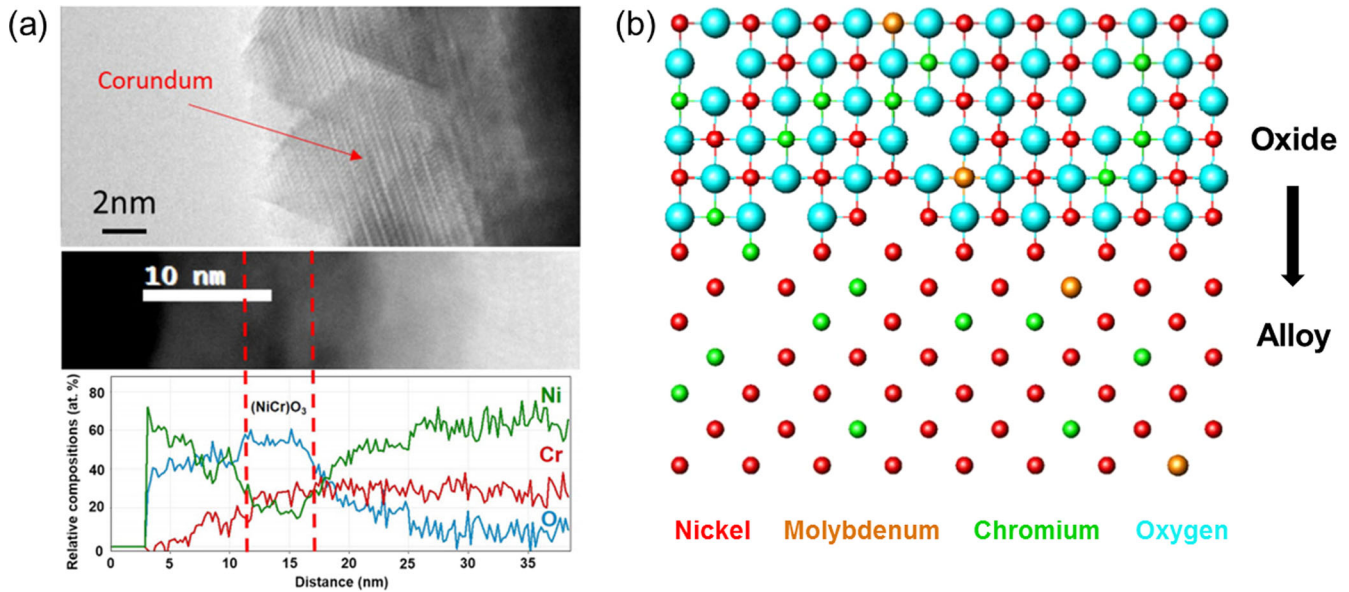


**Fig. 10** Microstructure analysis of surface oxide film formed on  $\text{Ni}_{72}\text{Cr}_{22}\text{Mo}_6$  alloy oxidized in situ at 700 °C in an oxygen environment. **a** A bright field image of  $\text{Ni}_{72}\text{Cr}_{22}\text{Mo}_6$  sample, showing fringes characteristic of the corundum structure adjacent to the metal. A high-angle annular dark field image with the corresponding electron energy loss line scan, showing the corundum structure adjacent to the metal has a composition of approximately  $\text{CrNiO}_3$ . **b** Diagram of an oxidation front with a rocksalt oxide moving into an alloy with a velocity  $v$ , with the different types of atoms color-coded, with a number of metal vacancies<sup>69</sup>. (The American Physical Society Copyright, Order identification number RNP/23/SEP/070493, <https://powereditor.aptaarcop.com/sciprisaps/RnPRequest/ViewRequest?Collection=T48pzZLYz1s%3d>).

oxide films that grew on the surfaces of the grains with different crystal orientations in the NiCr binary alloy had markedly different structures and compositions. A solute that captured rock salt oxides formed with a cube-cube epitaxial orientation on the (100) oriented grains, while a solute that captured corundum oxides formed, with the (0001) basal plane parallel to the (111) oriented grain. For the (100) plane, the oxide composition at the alloy/oxide interface was controlled by how rapidly the cations crossed the interface versus exchanged with the alloy. For the (111) plane, it was controlled by cation addition at the interface versus exchange across the interface. The surface passive films formed by galvanostat experiments in 0.1 M deaerated NaCl solution on NiCr and NiCrMo alloys were studied by TEM<sup>140</sup>. Compared to the chemical composition of rock salt oxide on the top layer for NiCr alloy, the corundum in the external oxide layer for NiCrMo alloy contains obviously more Ni by EDS line scanning, as shown in Supplementary Fig. 5. The results confirmed that Mo addition promoted the formation of a metastable corundum phase as a consequence of nonequilibrium solute capture of Ni in corundum. The external corundum oxide layer could change the transport mechanism as well as the diffusivity of oxygen through the passive film and across the metal/oxide interface, thus changing the localized oxygen penetration and improving the passive film protectiveness. Under high-temperature oxidation conditions, compared to the NiCr alloy, Mo doping possibly stabilized the cation vacancies and inhibited Kirkendall void formation by promoting the nucleation of the metastable  $\text{Ni}_{2-x}\text{Cr}_x\text{O}_3$  corundum structure phase at the metal/oxide interface for the NiCrMo alloy<sup>141</sup>. Therefore, nonequilibrium solute capture during oxide film growth controlled by diffusion dynamics was a general phenomenon independent of whether the oxides formed by dry oxidation under high temperature or in aqueous conditions. Studying the structure of oxide and the sequence of phase nucleation during the high-temperature oxidation could help to understand the migration in the mass transportation process, which was important to understand the morphological stability and breakdown mechanism of protective passive film on alloy surface.

Thus, the formation of multi-element oxides was related to the occurrence of nonequilibrium solute capture during oxide film growth. The nonequilibrium solute capture leads to the trapping of large dopant concentrations in the oxide, which could affect the protectiveness of passive film against breakdown in corrosive environments<sup>142</sup>. The dopant cation has a lower valence state, such as Al-doped  $\text{TiO}_2$ <sup>143</sup> and Ni-doped  $\text{Cr}_2\text{O}_3$ <sup>144</sup>, which has been shown to promote an increase in positively charged oxygen vacancies, in order to increase the electron charge carriers to maintain charge neutrality of the passive film. For the situation where  $\text{Mo}^{6+}$  is substituted onto a  $\text{Ni}^{2+}$  or  $\text{Cr}^{3+}$  lattice site<sup>142</sup>, and  $\text{Nb}^{5+}$  is substituted onto a  $\text{Ti}^{4+}$  lattice site<sup>145,146</sup>, the net positive charge would result in the annihilation of electron holes and attraction of negatively charged defects, such as cation vacancies. Shuang et al.<sup>147</sup> found that the chemically complex multi-element oxide film containing all alloying elements that formed on the  $\text{FeCrNiCoNb}_{0.5}$  MPEAs was a less defective or a more compact amorphous structure, which contributed to high anti-corrosion performance. Thus, the composition and structure of the formed multi-element oxides were complex, as some factors were at play, such as the oxidation temperature, bulk alloy composition, grain orientation, selective oxidation at the metal/oxide interface, the diffusion coefficient of the cations in the oxide, and cation doping through substitution into a host oxide lattice.

#### OPEN QUESTIONS

The passivation ability and stability of the formed passive film have significant effects on the corrosion resistance of the MPEAs. In-depth research on the passivation mechanism will be helpful in understanding the specific role of constituent elements in the passive film formation process. It is extremely challenging to select an appropriate composition to optimize the protectiveness of passive films for different corrosion environments by trial-and-error experiments. The composition and structure of surface oxides affected by alloy composition and selective oxidation are complex and play an important role in the corrosion resistance of

MPEAs. Some key issues for exploration are summarized as follows.

(1) What are the contributions of individual alloying elements or synergistic effects between the elements on the improved protectiveness of the passive film on an MPEA substrate? The corrosion resistance of the passive film will be determined by the dissolution rate of surface oxides and the vulnerability to pitting corrosion. Therefore, it is necessary to determine whether the main contribution of specified alloying element addition will slow down the chemical dissolution of the passive film or improve the pitting resistance of the passive film.

(2) What is the critical concentration of a single passivating element or optimal combination of elements that needs to be applied, to a large degree, to optimize the corrosion resistance of a passive film on MPEAs under a condition where the alloy composition will be systematically altered without changing alloy phase structure?

(3) For the MPEAs, how does selective dissolution at active surfaces or oxide/electrolyte interfaces contribute to surface modification and multi-element oxide formation? How does each element contribute to the passivation mechanism and dissolution kinetics characteristic of the MPEAs?

(4) How does the formation of phase-separated or complex multi-principal oxides contribute to the corrosion and oxidation resistance of MPEAs?

(5) What are the composition and structure of initially formed complex multi-principal oxides, and how do they evolve with time? Will the cation substitution process occur, and whether it will affect the ionic and electronic defect concentrations in the oxide?

(6) How do changes in alloy composition affect the synergistic effect of multiple principal components, thereby altering the cation dissolution kinetics and microstructure of the passive film, which is crucial for revealing the uniform corrosion and pitting resistance mechanisms of MPEAs?

## SUMMARY AND OUTLOOK

Emerging MPEAs open up a large compositional space, with the possibility of complex oxides with enhanced passivity properties, demonstrating excellent corrosion and oxidation resistance. The stability of passive film, passivation mechanism, and surface oxide film characteristics of the MPEAs, have been preliminarily studied. (1) The formation of stable passive film was found to be dependent on the microstructure of the MPEAs with a single-phase structure and uniform elemental distribution. It is necessary to use machine learning, phase diagram calculations, and high-throughput technology to comprehensively and efficiently optimize the microstructures of MPEAs, to improve the protectiveness of passive films. From the research results on the influence of alloying elements on the corrosion resistance of MPEAs, Cr was found to be the most important passivating element. The stability of the passive film on MPEAs was found to be significantly affected by the concentration and distribution uniformity of Cr in the passive film and by the influence of other elements, such as Al, Ni, Mo, Co, and Ti coupled with Cr, which influenced the occurrence of galvanic corrosion. In general, the addition of Mo and Co could enhance the stability of  $\text{Cr}_2\text{O}_3$ , improving the protectiveness of the passive film, while the introduction of Mn and Al could decrease the concentrations of  $\text{Cr}_2\text{O}_3$ , with a deleterious effect on passive film stability. The addition of Mo was found to provide a tremendous beneficial effect on the corrosion properties with the formation of a passive film resistant to pitting corrosion. (2) For the MPEAs, elements dissolved incongruently, modifying the surface chemistry and leading to the enrichment or accumulation of elements in an oxidized state on the surface at the open-circuit potential or a given potential, which could be determined by in situ AESEC. The preferential dissolution of Ni in the oxides of some MPEAs consisted of transition metal

elements, such as NiCr, NiCrMo, and CoCrFeNiMn, which was confirmed by AESEC analysis, thus causing a significant lack of Ni in the oxide film. The preferential dissolution of some specific elements in the MPEAs could increase the defect density in the oxide, thus providing an easy path for the oxygen to migrate in and assist in the growth of oxides of other elements. Many important aspects of passivity including transpassive dissolution and repassivation behavior associated with elements' selective dissolution and reprecipitation characteristics, should be studied on MPEAs. Further experiments using AESEC combined with the analysis of oxide composition using XPS and 3D-APT are needed to understand the correlation of preferential element release, the bonding environment, formation mechanisms, and passivity of these oxide films, as well as their impacts on the corrosion kinetics and material chemical durability. (3) The formation of phase-separated oxides, such as layered oxide structures and embedded oxide structures, on MPEAs was found to be the result of selective oxidation of elements at the metal/oxide interface, differential cation transport rates across the oxides, the interactions between constituent elements, and the formation of some alloy phases due to the dealloying process. (4) The oxides were found to grow too fast or the fluxes through the interface were too large for local interfacial equilibrium to exist, resulting in the occurrence of nonequilibrium solute capture. The formation of non-stoichiometric multi-element oxides was found to be related to nonequilibrium solute capture, which occurred at the interface of the alloy/film during oxide growth and was controlled by a combination of thermodynamics and kinetics. For the MPEAs, determining whether high-entropy oxides containing many elements with one phase are thermodynamically stable needs to be further studied. Multi-element oxide databases also need to be established based on the CALculation of PHase Diagram method to understand the corrosion or oxidation of MPEAs. The stability of solid solution oxide compositions based on common crystal structures, such as corundum, spinels, and rock salt, will have to be further explored, through modern high-resolution microscopy techniques such as STEM and 3D-APT, to determine whether the cocktail effect of these multi-element oxides with a very wide range of compositions can lead to lower diffusion rates or influence the transport mechanism of the existing point defects, and this may present kinetic barriers to enhance the corrosion or oxidation resistance of MPEAs.

## DATA AVAILABILITY

Data sharing is not applicable to this article as no datasets were generated or analyzed during the current study.

## CODE AVAILABILITY

Not applicable.

Received: 18 June 2023; Accepted: 23 October 2023;

Published online: 06 November 2023

## REFERENCES

- Shi, Y., Yang, B. & Liaw, P. K. Corrosion-resistant high-entropy alloys: a review. *Metals* **7**, 43 (2017).
- Qiu, Y., Thomas, S., Gibson, M. A., Fraser, H. L. & Birbilis, N. Corrosion of high entropy alloys. *Npj Mater. Degrad.* **1**, 1–18 (2017).
- Tang, Z., Huang, L., He, W. & Liaw, P. K. Alloying and processing effects on the aqueous corrosion behavior of high-entropy alloys. *Entropy* **16**, 895–911 (2014).
- Qiu, Y., Gibson, M., Fraser, H. & Birbilis, N. Corrosion characteristics of high entropy alloys. *Mater. Sci. Technol.* **31**, 1235–1243 (2015).
- Nascimento, C. B., Donatus, U., Rios, C. T., Oliveir, a M.C.L.d. & Antunes, R. A. A review on corrosion of high entropy alloys: exploring the interplay between corrosion properties, alloy composition, passive film stability and materials selection. *Mater. Res.* **25**, e20210442 (2022).

6. Fu, Y., Li, J., Luo, H., Du, C. & Li, X. Recent advances on environmental corrosion behavior and mechanism of high-entropy alloys. *J. Mater. Sci. Technol.* **80**, 217–233 (2021).
7. Yang, J. et al. Effects of Mn on the electrochemical corrosion and passivation behavior of CoFeNiMnCr high-entropy alloy system in H<sub>2</sub>SO<sub>4</sub> solution. *J. Alloy. Compd.* **819**, 152943 (2020).
8. Dai, C., Zhao, T., Du, C., Liu, Z. & Zhang, D. Effect of molybdenum content on the microstructure and corrosion behavior of FeCoCrNiMo<sub>x</sub> high-entropy alloys. *J. Mater. Sci. Technol.* **46**, 64–73 (2020).
9. Shi, Y., Collins, L., Balke, N., Liaw, P. K. & Yang, B. In-situ electrochemical-AFM study of localized corrosion of Al<sub>x</sub>CoCrFeNi high-entropy alloys in chloride solution. *Appl. Surf. Sci.* **439**, 533–544 (2018).
10. Muangtong, P., Rodchanarowan, A., Chaysuwan, D., Chanlek, N. & Goodall, R. The corrosion behaviour of CoCrFeNi-x (x = Cu, Al, Sn) high entropy alloy systems in chloride solution. *Corros. Sci.* **172**, 108740 (2020).
11. Chai, W., Lu, T. & Pan, Y. Corrosion behaviors of FeCoNiCr<sub>x</sub> (x = 0, 0.5, 1.0) multi-principal element alloys: role of Cr-induced segregation. *Intermetallics* **116**, 106654 (2020).
12. Lu, P. et al. Computational design and initial corrosion assessment of a series of non-equimolar high entropy alloys. *Scr. Mater.* **172**, 12–16 (2019).
13. Yang, S. et al. Effect of Cr content on corrosion behavior of AlCr<sub>x</sub>FeNi<sub>2</sub>Cu<sub>1.6</sub> high entropy alloys. *Mater. Res. Express* **6**, 076501 (2019).
14. Wang, W. et al. Effect of Mo and aging temperature on corrosion behavior of (CoCrFeNi)<sub>100-x</sub>Mo<sub>x</sub> high-entropy alloys. *J. Alloy. Compd.* **812**, 152139 (2020).
15. Godlewska, E. M. et al. Corrosion of Al(Co)CrFeNi high-entropy alloys. *Front. Mater.* **7**, 566336 (2020).
16. Zhao, R. F. et al. Corrosion behavior of Co<sub>x</sub>CrCuFeMnNi high-entropy alloys prepared by hot pressing sintered in 3.5% NaCl solution. *Results Phys.* **15**, 102667 (2019).
17. Qiu, X. W. & Liu, C. G. Microstructure and properties of Al<sub>2</sub>CrFeCoCuTiNi<sub>x</sub> high-entropy alloys prepared by laser cladding. *J. Alloy. Compd.* **553**, 216–220 (2013).
18. López Ríos, M. et al. Effects of nickel content on the microstructure, micro-hardness and corrosion behavior of high-entropy AlCoCrFeNi<sub>x</sub> alloys. *Sci. Rep.* **10**, 1–11 (2020).
19. Han, Z. et al. Structures and corrosion properties of the AlCrFeNiMo<sub>0.5</sub>Ti<sub>x</sub> high entropy alloys. *Mater. Corros.* **69**, 641–647 (2018).
20. Shi, H. et al. Influence of alloying elements (Cu, Ti, Nb) on the microstructure and corrosion behaviour of AlCrFeNi-based high entropy alloys exposed to oxygen-containing molten Pb. *Corros. Sci.* **190**, 109659 (2021).
21. Wang, X. Z., Hu, Q., Zhang, L. & Cui, Z. The influence of Nb addition on the passivity of CoCrNiNb<sub>x</sub> multi-principal element alloys. *J. Electroanal. Chem.* **908**, 116107 (2022).
22. Liu, C. et al. Effect of Nb content on the microstructure and corrosion resistance of FeCoCrNiNb<sub>x</sub> high-entropy alloys in chloride ion environment. *J. Alloy. Compd.* **935**, 168013 (2023).
23. Hsu, Y. J., Chiang, W. C. & Wu, J. K. Corrosion behavior of FeCoNiCrCu<sub>x</sub> high-entropy alloys in 3.5% sodium chloride solution. *Mater. Chem. Phys.* **92**, 112–117 (2005).
24. Peng, Z. et al. A lightweight AlCrTiV<sub>0.5</sub>Cu<sub>x</sub> high-entropy alloy with excellent corrosion resistance. *Materials* **16**, 2922 (2023).
25. Lee, C., Chang, C., Chen, Y., Yeh, J. & Shih, H. Effect of the aluminium content of Al<sub>x</sub>CrFe<sub>1.5</sub>MnNi<sub>0.5</sub> high-entropy alloys on the corrosion behaviour in aqueous environments. *Corros. Sci.* **50**, 2053–2060 (2008).
26. Shi, Y. et al. Homogenization of Al<sub>x</sub>CoCrFeNi high-entropy alloys with improved corrosion resistance. *Corros. Sci.* **133**, 120–131 (2018).
27. Shi, Y. et al. Corrosion of Al<sub>x</sub>CoCrFeNi high-entropy alloys: Al-content and potential scan-rate dependent pitting behavior. *Corros. Sci.* **119**, 33–45 (2017).
28. Gu, X. H. et al. Microstructure characterization and corrosion behavior of Al<sub>x</sub>(CoCrFeNi)<sub>100-x</sub> (x = 0, 5, 10, 15, 20) high entropy alloys in 0.5 M H<sub>2</sub>SO<sub>4</sub> solution. *J. Alloy. Compd.* **944**, 169247 (2023).
29. Wang, C. et al. Microstructure and corrosion properties of laser remelted CrFeCoNi and CrMnFeCoNi high entropy alloys coatings. *J. Mater. Res. Technol.* **15**, 5187–5196 (2021).
30. Hsu, K. M., Chen, S. H. & Lin, C. S. Microstructure and corrosion behavior of FeCrNiCoMn<sub>x</sub>(x = 1.0, 0.6, 0.3, 0) high entropy alloys in 0.5 M H<sub>2</sub>SO<sub>4</sub>. *Corros. Sci.* **190**, 109694 (2021).
31. Li, T. et al. Localized corrosion behavior of a single-phase non-equimolar high entropy alloy. *Electrochim. Acta* **306**, 71–84 (2019).
32. Zhang, P. et al. A high-corrosion-resistant high-entropy alloys (HEAs) coatings with single BCC solid solution structure by laser remelting. *Mater. Lett.* **324**, 132728 (2022).
33. Marcus, P. et al. Enhanced passivity and resistance to pitting of new Cr-Fe-Co-Ni-Mo multi-principal element single-phase alloys. *ECS Meet. Abstr.* **242**, 732–732 (2022).
34. Senkov, O. N., Miracle, D. B., Chaput, K. J. & Couzine, J. P. Development and exploration of refractory high entropy alloys-A review. *J. Mater. Res.* **33**, 3092–3128 (2018).
35. Zhou, J. L., Cheng, Y. H., Chen, Y. X. & Liang, X. B. Composition design and preparation process of refractory high-entropy alloys: a review. *Int. J. Refract. Met. Hard Mater.* **105**, 105836 (2022).
36. Xiong, W. et al. Refractory high-entropy alloys: a focused review of preparation methods and properties. *J. Mater. Sci. Technol.* **142**, 196–215 (2023).
37. Hua, X. J. et al. Development and property tuning of refractory high-entropy alloys: a review. *Acta Metall. Sin. (Engl. Lett.)* **35**, 1231–1265 (2022).
38. Xie, X. et al. Research progress of refractory high entropy alloys: a review. *Chin. J. Mech. Eng.* **35**, 142 (2022).
39. Srikanth, M., Annamalai, A. R., Muthuchamy, A. & Jen, C. P. A review of the latest developments in the field of refractory high-entropy alloys. *Crystals* **11**, 612 (2021).
40. Yao, H. et al. NbTaV-(Ti, W) refractory high-entropy alloys: experiments and modeling. *Mater. Sci. Eng. A.* **674**, 203–211 (2016).
41. Coury, F. G., Kaufman, M. & Clarke, A. J. Solid-solution strengthening in refractory high entropy alloys. *Acta Mater.* **175**, 66–81 (2019).
42. Soni, V. et al. Phase stability as a function of temperature in a refractory high-entropy alloy. *J. Mater. Res.* **33**, 3235–3246 (2018).
43. Yao, J. et al. Phase stability of a ductile single-phase BCC Hf<sub>0.5</sub>Nb<sub>0.5</sub>Ta<sub>0.5</sub>Ti<sub>1.5</sub>Zr refractory high-entropy alloy. *Intermetallics* **98**, 79–88 (2018).
44. Wang, K., Han, J., Gerard, A. Y., Scully, J. R. & Zhou, B. C. Potential-pH diagrams considering complex oxide solution phases for understanding aqueous corrosion of multi-principal element alloys. *Npj Mater. Degrad.* **4**, 1–11 (2020).
45. Lu, P. et al. Computational materials design of a corrosion resistant high entropy alloy for harsh environments. *Scr. Mater.* **153**, 19–22 (2018).
46. Scully, J. R. et al. Controlling the corrosion resistance of multi-principal element alloys. *Scr. Mater.* **188**, 96–101 (2020).
47. Birbilis, N., Choudhary, S., Scully, J. & Taheri, M. A perspective on corrosion of multi-principal element alloys. *Npj Mater. Degrad.* **5**, 1–8 (2021).
48. Hurley, P. K. et al. The characterization and passivation of fixed oxide charges and interface states in the MOS system. *IEEE Trans. Device Mater. Reliab.* **13**, 429–443 (2013).
49. Clayton, C. & Lu, Y. A bipolar model of the passivity of stainless steel: the role of Mo addition. *J. Electrochem. Soc.* **133**, 2465 (1986).
50. Marcus, P. On some fundamental factors in the effect of alloying elements on passivation of alloys. *Corros. Sci.* **36**, 2155–2158 (1994).
51. Urquidí-Macdonald, M. & Macdonald, D. D. Theoretical analysis of the effects of alloying elements on distribution functions of passivity breakdown. *J. Electrochem. Soc.* **136**, 961 (1989).
52. Qiu, Y. et al. Microstructure and corrosion properties of the low-density single-phase compositionally complex alloy AlTiVCr. *Corros. Sci.* **133**, 386–396 (2018).
53. Zheng, S., Cai, Z., Pu, J., Zeng, C. & Wang, L. Passivation behavior of VAlTiCrSi amorphous high-entropy alloy film with a high corrosion-resistance in artificial sea water. *Appl. Surf. Sci.* **542**, 148520 (2021).
54. Han, J. et al. Potential dependent Mn oxidation and its role in passivation of Ni<sub>38</sub>Fe<sub>20</sub>Cr<sub>22</sub>Mn<sub>10</sub>Co<sub>10</sub> multi-principal element alloy using multi-element resolved atomic emission spectroelectrochemistry. *J. Electrochem. Soc.* **168**, 051508 (2021).
55. Henderson, J. D. et al. Investigating the role of Mo and Cr during the activation and passivation of Ni-based alloys in acidic chloride solution. *J. Electrochem. Soc.* **168**, 021509 (2021).
56. Choudhary, S. et al. On the dynamic passivity and corrosion resistance of a low cost and low density multi-principal-element alloy produced via commodity metals. *Electrochem. Commun.* **125**, 106989 (2021).
57. Laplanche, G., Volkert, U., Eggeler, G. & George, E. Oxidation behavior of the CrMnFeCoNi high-entropy alloy. *Oxid. Met.* **85**, 629–645 (2016).
58. Seyeux, A. et al. ToF-SIMS investigation with 18O isotopic tracer of the ion transport mechanisms in surface oxides on nickel-chromium and nickel-chromium-molybdenum alloys. *Electrochim. Acta* **426**, 140797 (2022).
59. Zhang, B. et al. Quasi-in-situ observing the growth of native oxide film on the FeCr<sub>15</sub>Ni<sub>15</sub> austenitic alloy by TEM. *Corros. Sci.* **140**, 1–7 (2018).
60. Li, Y., Kostka, A., Savan, A. & Ludwig, A. Atomic-scale investigation of fast oxidation kinetics of nanocrystalline CrMnFeCoNi thin films. *J. Alloy. Compd.* **766**, 1080–1085 (2018).
61. Wang, L. et al. Study of the surface oxides and corrosion behaviour of an equiatomic CoCrFeMnNi high entropy alloy by XPS and ToF-SIMS. *Corros. Sci.* **167**, 108507 (2020).
62. Wang, L. et al. Insight on passivity of high entropy alloys: Thermal stability and ion transport mechanisms in the passive oxide film on CoCrFeMnNi surfaces. *Corros. Sci.* **188**, 109540 (2021).
63. Wang, X. et al. Origin of enhanced passivity of Cr-Fe-Co-Ni-Mo multi-principal element alloy surfaces. *Npj Mater. Degrad.* **7**, 13 (2023).
64. Gerard, A. Y. et al. Aqueous passivation of multi-principal element alloy Ni<sub>38</sub>Fe<sub>20</sub>Cr<sub>22</sub>Mn<sub>10</sub>Co<sub>10</sub>: Unexpected high Cr enrichment within the passive film. *Acta Mater.* **198**, 121–133 (2020).

65. Kautz, E. J. et al. Element redistributions during early stages of oxidation in a  $\text{Ni}_{38}\text{Cr}_{22}\text{Fe}_{20}\text{Mn}_{10}\text{Co}_{10}$  multi-principal element alloy. *Scr. Mater.* **194**, 113609 (2021).
66. Schreiber, D. K. et al. Revealing the complexity of high temperature oxide formation in a 38Ni-21Cr-20Fe-13Ru-6Mo-2W (at.%) multi-principal element alloy. *Scr. Mater.* **210**, 114419 (2022).
67. Yu, X. X., Taylor, M. A., Perepezko, J. H. & Marks, L. D. Competition between thermodynamics, kinetics and growth mode in the early-stage oxidation of an equimolar CoCrFeNi alloy. *Acta Mater.* **196**, 651–659 (2020).
68. Quiambao, K. F. et al. Passivation of a corrosion resistant high entropy alloy in non-oxidizing sulfate solutions. *Acta Mater.* **164**, 362–376 (2019).
69. Yu, X. X. et al. Nonequilibrium solute capture in passivating oxide films. *Phys. Rev. Lett.* **121**, 145701 (2018).
70. Newman, R., Meng, F. T. & Sieradzki, K. Validation of a percolation model for passivation of Fe-Cr alloys: I current efficiency in the incompletely passivated state. *Corros. Sci.* **28**, 523–527 (1988).
71. Uhlig, H. H. & Woodside, G. E. Anodic polarization of passive and non-passive chromium-iron alloys. *J. Phys. Chem.* **57**, 280–283 (1953).
72. Ferrari, A. & Körmann, F. Surface segregation in Cr-Mn-Fe-Co-Ni high entropy alloys. *Appl. Surf. Sci.* **533**, 147471 (2020).
73. Shang, X. et al. The intrinsic mechanism of corrosion resistance for FCC high entropy alloys. *Sci. China Technol. Sci.* **61**, 189–196 (2018).
74. Yan, X. et al.  $\text{Al}_{0.3}\text{Cr}_x\text{FeCoNi}$  high-entropy alloys with high corrosion resistance and good mechanical properties. *J. Alloy. Compd.* **860**, 158436 (2021).
75. Han, Z. et al. The corrosion behavior of ultra-fine grained CoNiFeCrMn high-entropy alloys. *J. Alloy. Compd.* **816**, 152583 (2020).
76. Huang, L., Wang, X., Zhao, X., Wang, C. & Yang, Y. Analysis on the key role in corrosion behavior of CoCrNiAlTi-based high entropy alloy. *Mater. Chem. Phys.* **259**, 124007 (2021).
77. Pardo, A. et al. Pitting corrosion behaviour of austenitic stainless steels—combining effects of Mn and Mo additions. *Corros. Sci.* **50**, 1796–1806 (2008).
78. Hashimoto, K., Asami, K. & Teramoto, K. An X-ray photo-electron spectroscopic study on the role of molybdenum in increasing the corrosion resistance of ferritic stainless steels in HCl. *Corros. Sci.* **19**, 3–14 (1979).
79. Montemor, M., Simões, A., Ferreira, M. & Belo, M. D. C. The role of Mo in the chemical composition and semiconductive behaviour of oxide films formed on stainless steels. *Corros. Sci.* **41**, 17–34 (1999).
80. Dou, Y., Han, S., Wang, L., Wang, X. & Cui, Z. Characterization of the passive properties of 254SMO stainless steel in simulated desulfurized flue gas condensates by electrochemical analysis, XPS and ToF-SIMS. *Corros. Sci.* **165**, 108405 (2020).
81. Li, Y. et al. Effects of partially substituting cobalt for nickel on the corrosion resistance of a Ni-16Cr-15Mo alloy to aqueous hydrofluoric acid. *Corros. Sci.* **78**, 101–110 (2014).
82. Hu, Q. et al. Mo content-dependent competition between  $\text{Cr}_2\text{O}_3$  enrichment and selective dissolution of CoCrFeNiMo<sub>x</sub> high entropy alloys. *Npj Mater. Degrad.* **6**, 97 (2022).
83. Shuang, S. et al. Unusually high corrosion resistance in Mo<sub>x</sub>CrNiCo medium entropy alloy enhanced by acidity in aqueous solution. *J. Mater. Sci. Technol.* **139**, 59–68 (2023).
84. Li, X. et al. The contribution of Cr and Mo to the passivation of Ni22Cr and Ni22Cr10Mo alloys in sulfuric acid. *Corros. Sci.* **176**, 109015 (2020).
85. Chen, J. et al. Effects of alloying concentration on the aqueous corrosion and passivation of aluminum-manganese-molybdenum concentrated alloys. *Corros. Sci.* **198**, 110137 (2022).
86. Wang, X. et al. Enhanced passivity of Cr-Fe-Co-Ni-Mo multi-component single-phase face-centred cubic alloys: design, production and corrosion behaviour. *Corros. Sci.* **200**, 110233 (2022).
87. Pardo, A. et al. Effect of Mo and Mn additions on the corrosion behaviour of AISI 304 and 316 stainless steels in  $\text{H}_2\text{SO}_4$ . *Corros. Sci.* **50**, 780–794 (2008).
88. Park, K. & Kwon, H. Effects of Mn on the localized corrosion behavior of Fe-18Cr alloys. *Electrochim. Acta* **55**, 3421–3427 (2010).
89. Torbati-Sarraf, H., Shabani, M., Jablonski, P. D., Pataky, G. J. & Poursae, A. The influence of incorporation of Mn on the pitting corrosion performance of CrFeCoNi High Entropy Alloy at different temperatures. *Mater. Des.* **184**, 108170 (2019).
90. Liu, J. C. & Zhang, G. Effect of trace Mn modification on the microstructure and corrosion behavior of Sn-9Zn solder alloy. *Mater. Corros.* **69**, 781–792 (2018).
91. Qiu, J. et al. Corrosion behaviour and surface analysis of a Co-Cr and two Ni-Cr dental alloys before and after simulated porcelain firing. *Eur. J. Oral Sci.* **119**, 93–101 (2011).
92. Qiu, X. W., Wu, M. J., Liu, C. G., Zhang, Y. P. & Huang, C. X. Corrosion performance of  $\text{Al}_2\text{CrFeCo}_x\text{CuNiTi}$  high-entropy alloy coatings in acid liquids. *J. Alloy. Compd.* **708**, 353–357 (2017).
93. Yen, C. C. et al. Corrosion mechanism of annealed equiatomic AlCoCrFeNi tri-phase high-entropy alloy in 0.5 M  $\text{H}_2\text{SO}_4$  aerated aqueous solution. *Corros. Sci.* **157**, 462–471 (2019).
94. Wei, R. et al. The effect of Co substitutions for Ni on microstructure, mechanical properties and corrosion resistance of  $\text{Fe}_{50}\text{Mn}_{25}\text{Cr}_{15}\text{Ni}_{10}$  medium-entropy alloy. *Intermetallics* **149**, 107654 (2022).
95. Alqarni, N. D. et al. Effect of cobalt addition on the corrosion behavior of near equiatomic NiTi shape memory alloy in normal saline solution: Electrochemical and XPS studies. *RSC Adv.* **8**, 19289–19300 (2018).
96. Wu, P., Gan, K., Yan, D., Fu, Z. & Li, Z. A non-equiatomic FeNiCoCr high-entropy alloy with excellent anti-corrosion performance and strength-ductility synergy. *Corros. Sci.* **183**, 109341 (2021).
97. Shi, Y. et al. High-throughput synthesis and corrosion behavior of sputter-deposited nanocrystalline  $\text{Al}_x(\text{CoCrFeNi})_{100-x}$  combinatorial high-entropy alloys. *Mater. Des.* **195**, 109018 (2020).
98. Nascimento, C. B., Donatus, U., Rios, C. T. & Antunes, R. A. Electronic properties of the passive films formed on CoCrFeNi and CoCrFeNiAl high entropy alloys in sodium chloride solution. *J. Mater. Res. Technol.* **9**, 13879–13892 (2020).
99. Raza, A., Abdulahad, S., Kang, B., Ryu, H. J. & Hong, S. H. Corrosion resistance of weight reduced  $\text{Al}_x\text{CrFeMoV}$  high entropy alloys. *Appl. Surf. Sci.* **485**, 368–374 (2019).
100. Pan, Z. et al. Tailoring microstructure and corrosion behavior of CoNiAl<sub>x</sub> medium entropy alloys via Al addition. *Corros. Sci.* **207**, 110570 (2022).
101. Fu, Y. et al. The corrosion behavior and film properties of Al-containing high-entropy alloys in acidic solutions. *Appl. Surf. Sci.* **560**, 149854 (2021).
102. Wu, M., Setiawan, R. C. & Li, D. Benefits of passive element Ti to the resistance of AlCrFeCoNi high-entropy alloy to corrosion and corrosive wear. *Wear* **492**, 204231 (2022).
103. Gu, X., Zhuang, Y. & Huang, D. Corrosion behaviors related to the microstructural evolutions of as-cast  $\text{Al}_{0.3}\text{CoCrFeNi}$  high entropy alloy with addition of Si and Ti elements. *Intermetallics* **147**, 107600 (2022).
104. Zhao, Y. et al. Effects of Ti-to-Al ratios on the phases, microstructures, mechanical properties, and corrosion resistance of  $\text{Al}_{2-x}\text{CoCrFeNiTi}_x$  high-entropy alloys. *J. Alloy. Compd.* **805**, 585–596 (2019).
105. Yang, J. et al. Enhanced electromagnetic-wave absorbing performances and corrosion resistance via tuning Ti contents in FeCoNiCuTi<sub>x</sub> high-entropy alloys. *ACS Appl. Mater. Interfaces* **14**, 12375–12384 (2022).
106. Wang, X. et al. Effect of Ti content on the microstructure and corrosion resistance of CoCrFeNiTi<sub>x</sub> high entropy alloys prepared by laser cladding. *Materials* **13**, 2209 (2020).
107. Wen, X. et al. Corrosion and tribo-corrosion behaviors of nano-lamellar  $\text{Ni}_{1.5}\text{CrCoFe}_{0.5}\text{Mo}_{0.1}\text{Nb}_x$  eutectic high-entropy alloy coatings: The role of dual-phase microstructure. *Corros. Sci.* **201**, 110305 (2022).
108. Tanji, A., Fan, X., Sakidja, R., Liaw, P. K. & Hermawan, H. Niobium addition improves the corrosion resistance of TiHfZrNb<sub>x</sub> high-entropy alloys in Hanks' solution. *Electrochim. Acta* **424**, 140651 (2022).
109. Niu, Z. et al. Microstructure, mechanical properties and corrosion resistance of CoCrFeNiW<sub>x</sub> (x = 0, 0.2, 0.5) high entropy alloys. *Intermetallics* **112**, 106550 (2019).
110. Zhou, Z. et al. Effects of W addition on the corrosion behaviors of FeCoNiCrMn high entropy alloy composites in the 3.5 wt.% NaCl solution. *Surf. Interfaces* **23**, 100956 (2021).
111. Qi, W. et al. Effect of Zr on phase separation, mechanical and corrosion behavior of heterogeneous CoCrFeNiZr<sub>x</sub> high-entropy alloy. *J. Mater. Sci. Technol.* **109**, 76–85 (2022).
112. Brito-García, S., Mirza-Rosca, J., Geanta, V. & Voiculescu, I. Mechanical and corrosion behavior of Zr-doped high-entropy alloy from CoCrFeMoNi system. *Materials* **16**, 1832 (2023).
113. Yao, Y. et al. Corrosion behavior of AlFeCrCoNiZr<sub>x</sub> high-entropy alloys in 0.5 M sulfuric acid solution. *Metals* **11**, 1471 (2021).
114. Han, J. et al. Elementally resolved dissolution kinetics of a Ni-Fe-Cr-Mn-Co multi-principal element alloy in sulfuric acid using AESEC-EIS. *J. Electrochem. Soc.* **169**, 081507 (2022).
115. Lutton, K., Gusieva, K., Ott, N., Birbilis, N. & Scully, J. R. Understanding multi-element alloy passivation in acidic solutions using operando methods. *Electrochem. Commun.* **80**, 44–47 (2017).
116. Samin, A. J. & Taylor, C. D. First-principles investigation of surface properties and adsorption of oxygen on Ni-22Cr and the role of molybdenum. *Corros. Sci.* **134**, 103–111 (2018).
117. Henderson, J. D., Li, X., Shoesmith, D. W., Noël, J. J. & Ogle, K. Molybdenum surface enrichment and release during transpassive dissolution of Ni-based alloys. *Corros. Sci.* **147**, 32–40 (2019).
118. Choudhary, S., Qiu, Y., Thomas, S. & Birbilis, N. Element-resolved electrochemical analysis of transpassive dissolution and repassivation behavior of the multi-principal element alloy AlTiVCr. *Electrochim. Acta* **362**, 137104 (2020).
119. Qiu, Y. et al. Real-time dissolution of a compositionally complex alloy using inline ICP and correlation with XPS. *Npj Mater. Degrad.* **4**, 1–6 (2020).

120. Choudhary, S., Thomas, S., Macdonald, D. & Birbilis, N. Growth kinetics of multi-oxide passive film formed upon the multi-principal element alloy AlTiVCr: effect of transpassive dissolution of V and Cr. *J. Electrochem. Soc.* **168**, 051506 (2021).
121. Luo, H., Li, Z., Mingers, A. M. & Raabe, D. Corrosion behavior of an equiatomic CoCrFeMnNi high-entropy alloy compared with 304 stainless steel in sulfuric acid solution. *Corros. Sci.* **134**, 131–139 (2018).
122. Dworschak, D., Tseng, K. K., Yeh, J. W., Cheng, H. W. & Valtiner, M. Bottom-up characterization of electrochemical passivity from simple binary alloys to high entropy alloys. *Electrochim. Acta* **405**, 139804 (2022).
123. Sasidhar, K. et al. Understanding the protective ability of the native oxide on an Fe-13 at.% Cr alloy at the atomic scale: a combined atom probe and electron microscopy study. *Corros. Sci.* **211**, 110848 (2018).
124. Devaraj, A. et al. Visualizing the nanoscale oxygen and cation transport mechanisms during the early stages of oxidation of Fe-Cr-Ni alloy using in situ atom probe tomography. *Adv. Mater. Interfaces* **9**, 2200134 (2022).
125. Xu, Y. et al. Natural oxidation of amorphous  $\text{Cu}_x\text{Zr}_{1-x}$  alloys. *Appl. Surf. Sci.* **457**, 396–402 (2018).
126. Xu, Y. et al. On the competition between synchronous oxidation and preferential oxidation in Cu-Zr-Al metallic glasses. *Corros. Sci.* **177**, 108996 (2020).
127. Louzguine-Luzgin, D. et al. Bulk metallic glassy surface native oxide: Its atomic structure, growth rate and electrical properties. *Acta Mater.* **97**, 282–290 (2015).
128. Mendis, S. et al. Characteristics of oxide films on Ti-(10-75) Ta alloys and their corrosion performance in an aerated Hank's balanced salt solution. *Appl. Surf. Sci.* **506**, 145013 (2020).
129. Backman, L., Gild, J., Luo, J. & Opila, E. J. Part I: Theoretical predictions of preferential oxidation in refractory high entropy materials. *Acta Mater.* **197**, 20–27 (2020).
130. Gerard, A. Y. et al. The role of chromium content in aqueous passivation of a non-equiatomic  $\text{Ni}_{38}\text{Fe}_{20}\text{Cr}_x\text{Mn}_{21-0.5x}\text{Co}_{21-0.5x}$  multi-principal element alloy ( $x=22, 14, 10, 6$  at%) in acidic chloride solution. *Acta Mater.* **245**, 118607 (2023).
131. Kim, E. T. et al. Near atomic-scale comparison of passive film on a 17 wt% Cr-added 18 wt% Mn steel with those on typical austenitic stainless steels. *Scr. Mater.* **203**, 114112 (2021).
132. Zhang, B. et al. Unmasking chloride attack on the passive film of metals. *Nat. Commun.* **9**, 1–9 (2018).
133. Rost, C. M. et al. Entropy-stabilized oxides. *Nat. Commun.* **6**, 1–8 (2015).
134. Miracle, D. High entropy alloys as a bold step forward in alloy development. *Nat. Commun.* **10**(1), 3 (2019).
135. Hautier, G., Fischer, C., Ehrlicher, V., Jain, A. & Ceder, G. Data mined ionic substitutions for the discovery of new compounds. *Inorg. Chem.* **50**, 656–663 (2011).
136. Inman, S. B., Sur, D., Han, J., Ogle, K. & Scully, J. R. Corrosion behavior of a compositionally complex alloy utilizing simultaneous Al, Cr, and Ti passivation. *Corros. Sci.* **217**, 111138 (2023).
137. Hakiki, N. Comparative study of structural and semiconducting properties of passive films and thermally grown oxides on AISI 304 stainless steel. *Corros. Sci.* **53**, 2688–2699 (2011).
138. Wu, X., Voyshnis, S., Seyeux, A., Chumlyakov, Y. & Marcus, P. ToF-SIMS study of oxide films thermally grown on nickel-base alloys. *Corros. Sci.* **141**, 175–181 (2018).
139. Yu, X. X., Perepezko, J. H. & Marks, L. D. Crystallographic anisotropy of nonequilibrium solute capture. *Acta Mater.* **198**, 223–229 (2020).
140. Yu, X. X., Han, J., Scully, J. R. & Marks, L. D. Oxygen injection during fast vs slow passivation in aqueous solution. *Acta Mater.* **213**, 116898 (2021).
141. Yu, X. X. et al. In situ observations of early stage oxidation of Ni-Cr and Ni-Cr-Mo alloys. *Corrosion* **74**, 939–946 (2018).
142. Cwalina, K. L., Demarest, C., Gerard, A. & Scully, J. Revisiting the effects of molybdenum and tungsten alloying on corrosion behavior of nickel-chromium alloys in aqueous corrosion. *Curr. Opin. Solid State Mater. Sci.* **23**, 129–141 (2019).
143. Iwaszuk, A. & Nolan, M. Charge compensation in trivalent cation doped bulk rutile  $\text{TiO}_2$ . *J. Phys. Condens. Matter* **23**, 334207 (2011).
144. Carey, J. J., Legesse, M. & Nolan, M. Low valence cation doping of bulk  $\text{Cr}_2\text{O}_3$ : charge compensation and oxygen vacancy formation. *J. Phys. Chem. C* **120**, 19160–19174 (2016).
145. Zheng, L. et al. Investigation on the effect of Nb doping on the oxidation mechanism of  $\text{Ti}_3\text{SiC}_2$ . *Corros. Sci.* **140**, 374–378 (2018).
146. Nikolay, T., Larina, L., Shevaleevskiy, O. & Ahn, B. T. Electronic structure study of lightly Nb-doped  $\text{TiO}_2$  electrode for dye-sensitized solar cells. *Energy Environ. Sci.* **4**, 1480–1486 (2011).
147. Shuang, S., Ding, Z., Chung, D., Shi, S. & Yang, Y. Corrosion resistant nanostructured eutectic high entropy alloy. *Corros. Sci.* **164**, 108315 (2020).

## ACKNOWLEDGEMENTS

The authors would like to acknowledge the support of the National Natural Science Foundation of China under Grant No. 52371050.

## AUTHOR CONTRIBUTIONS

Z.W.: conceptualization, investigation, visualization, writing—original draft, writing—review & editing. Y.Y.: writing—review & editing, conceptualization, resources, funding acquisition, supervision. Y.W.: writing—review & editing. Y.Z.: writing—review & editing. X.Z.: writing—review & editing. Y.S.: investigation. L.Q.: resources, supervision.

## COMPETING INTERESTS

The authors declare no competing interests.

## ADDITIONAL INFORMATION

**Supplementary information** The online version contains supplementary material available at <https://doi.org/10.1038/s41529-023-00410-0>.

**Correspondence** and requests for materials should be addressed to Yu Yan.

**Reprints and permission information** is available at <http://www.nature.com/reprints>

**Publisher's note** Springer Nature remains neutral with regard to jurisdictional claims in published maps and institutional affiliations.



**Open Access** This article is licensed under a Creative Commons Attribution 4.0 International License, which permits use, sharing, adaptation, distribution and reproduction in any medium or format, as long as you give appropriate credit to the original author(s) and the source, provide a link to the Creative Commons license, and indicate if changes were made. The images or other third party material in this article are included in the article's Creative Commons license, unless indicated otherwise in a credit line to the material. If material is not included in the article's Creative Commons license and your intended use is not permitted by statutory regulation or exceeds the permitted use, you will need to obtain permission directly from the copyright holder. To view a copy of this license, visit <http://creativecommons.org/licenses/by/4.0/>.

© The Author(s) 2023